

3213

PRICE ET AL

SANDIA REPORT

SAND86-1131 • UC-70
Unlimited Release
Printed May 1987

JUN 02 1987

ADMINISTRATION

ANNA 870601-0063

Nevada Nuclear Waste Storage Investigations Project

Petrologic and Mechanical Properties of Outcrop Samples of the Welded, Devitrified Topopah Spring Member of the Paintbrush Tuff

SAIC/T&MSS

R. H. Price, J. R. Connolly, K. Keil

JUN 01 1987

CCF RECEIVED

Prepared by
Sandia National Laboratories
Albuquerque, New Mexico 87185 and Livermore, California 94550
for the United States Department of Energy
under Contract DE-AC04-76DP00789

"Prepared by Nevada Nuclear Waste Storage Investigations (NNWSI) Project participants as part of the Civilian Radioactive Waste Management Program (CRWM). The NNWSI Project is managed by the Waste Management Project Office (WMPO) of the U. S. Department of Energy, Nevada Operations Office (DOE/NV). NNWSI Project work is sponsored by the Office of Geologic Repositories (OGR) of the DOE Office of Civilian Radioactive Waste Management (OCRWM)."

Issued by Sandia National Laboratories, operated for the United States Department of Energy by Sandia Corporation.

NOTICE: This report was prepared as an account of work sponsored by an agency of the United States Government. Neither the United States Government nor any agency thereof, nor any of their employees, nor any of their contractors, subcontractors, or their employees, makes any warranty, express or implied, or assumes any legal liability or responsibility for the accuracy, completeness, or usefulness of any information, apparatus, product, or process disclosed, or represents that its use would not infringe privately owned rights. Reference herein to any specific commercial product, process, or service by trade name, trademark, manufacturer, or otherwise, does not necessarily constitute or imply its endorsement, recommendation, or favoring by the United States Government, any agency thereof or any of their contractors or subcontractors. The views and opinions expressed herein do not necessarily state or reflect those of the United States Government, any agency thereof or any of their contractors or subcontractors.

Printed in the United States of America
Available from
National Technical Information Service
U.S. Department of Commerce
5285 Port Royal Road
Springfield, VA 22161

NTIS price codes
Printed copy: A05
Microfiche copy: A01

SAND86-1131
Unlimited Release
Printed May 1987

Petrologic and Mechanical Properties of Outcrop Samples of the Welded, Devitrified Topopah Spring Member of the Paintbrush Tuff

R. H. Price
Geomechanics Division
Sandia National Laboratories
Albuquerque, New Mexico 87185

J. R. Connolly and K. Keil
Department of Geology
Institute of Meteoritics
University of New Mexico
Albuquerque, New Mexico 87131

ABSTRACT

More than fifty outcrop samples of the Topopah Spring Member of the Paintbrush Tuff have been analyzed for their petrologic or mechanical properties. In general, the compositions of these samples are very similar to each other and to stratigraphically equivalent samples from drill holes within Yucca Mountain. There are, however, specific textural features that are locally variable and a nonuniform distribution of high porosity textural features throughout Yucca Mountain. The mechanical test samples all had nominal diameters of 50.8 mm and a nominal length-to-diameter ratio of 2:1. Both fully saturated and oven dried samples were deformed in compression at effective confining pressures of 0, 5 and 10 MPa; temperatures of 22 and 150°C; and nominal strain rates of 10^{-7} , 10^{-5} , and 10^{-3} s^{-1} . Bulk modulus is directly related to both saturation and pressure, Young's modulus is inversely related to temperature, and ultimate strength is directly related to pressure and inversely related to temperature. All of these effects, however, are secondary to the elastic and strength property variability resulting from inclusion of highly porous inhomogeneities.

CONTENTS

INTRODUCTION	7
Sample Preparation	7
PETROLOGIC PROPERTIES	9
Petrography	9
Matrix Mineralogy and Composition	13
Estimation of Grain Densities from Mineralogic Data	16
MECHANICAL PROPERTIES	18
Experimental Techniques	18
Experimental Results	20
Discussion	23
CONCLUSIONS	27
REFERENCES	30
TABLES	34
FIGURES	44
APPENDIX A	59
APPENDIX B	70

TABLES

	PAGE
Table 1. Symbols, Definitions, Conventions and Units	34
Table 2. Brief Descriptions of the Mechanical Test Samples	35
Table 3. Summary of Mechanical Test Results	39
Table 4. Statistical Summary of Mechanical Property Data	42
Table 5. Coulomb Failure Criteria Values	43

FIGURES

	PAGE
Figure 1. Map of Nevada Test Site, Yucca Mountain, and Busted Butte	44
Figure 2. Molecular proportions of CaO, Na ₂ O, and K ₂ O in matrix	45
Figure 3. Composition of feldspar phenocrysts	46
Figure 4. Temperature-oxygen fugacity diagram	47
Figure 5. Plots of differential stress versus axial strain	48

INTRODUCTION

The U.S. Department of Energy is overseeing investigations of three different geologic units being considered for underground disposal of commercial nuclear wastes. One of the stratigraphic units under study is the Topopah Spring Member of the Paintbrush Tuff, which occurs within Yucca Mountain, near the southwest margin of the Nevada Test Site (NTS) in southern Nevada. Samples of the Topopah Spring Member are being tested for physical, thermal, and mechanical properties as part of the Nevada Nuclear Waste Storage Investigations (NNWSI) Project, which is administered by the Nevada Operations Office of the U.S. Department of Energy.

This is the second report presenting results of an integrated study of petrologic and mechanical properties of samples from the Topopah Spring Member (Price et al., 1985) and the eighth that presents data from mechanical tests conducted on intact (i.e., non-fractured) samples from the Topopah Spring Member (Olsson and Jones, 1980; Price, Nimick, and Zirzow, 1982; Price, Spence, and Jones, 1984; Price et al., 1985; Nimick et al., 1985; Price, 1986; Nimick, VanBuskirk, and MacFarland, in preparation). The test specimens used in this study were obtained from an outcrop on the southeast flank of Busted Butte. Petrographic properties presented here indicate that these samples are from a section of the Topopah Spring Member approximately stratigraphically equivalent to the proposed repository horizon within Yucca Mountain. The mechanical property data contained in this report ultimately will be used to aid in assessing the mineability and stability of underground openings in the Topopah Spring Member and to evaluate predicted near- and far-field responses to the presence of a repository within the unit. This laboratory mechanical test series was designed to study the effects of changes in water saturation, confining pressure, temperature, and strain rate on the deformation of intact, cylindrical samples with nominal diameters of 50.8 mm.

All symbols used in this report are listed in Table 1, where the terms are defined, conventions explained, and standard units assigned. The sample/test identifications used throughout this report consist of four, six, or seven numbers and letters.

Sample Preparation

Large irregular blocks were collected from an outcrop on the southeastern flank of Busted Butte, in the southwest corner of the Nevada Test Site, just east of the southern end of Yucca Mountain. The outcrop is located very close to north latitude $36^{\circ}46'19''$, west longitude $116^{\circ}25'28''$. The samples studied here are from the same block or from blocks adjacent to the block used to obtain samples for the sample size effect study (Price, 1986). A map locating the sampled outcrop is presented in Figure 1. A figure showing the stratigraphic setting of the Topopah Spring Member and a figure detailing

a measured section of the tuff exposures at the sample location can be found in Price (1986).

The samples were taken from a large block, designated Rock #10, excavated from a well exposed partial section of Topopah Spring Member near the southern end of Busted Butte. The block is part of a nominally nonlithophysal interval immediately below the upper-lithophysal zone. The block from which most of the samples were obtained is shown in Figure 2. The cut face from which cores were taken is designated face AE. Fifty-three 63.5 mm diameter cores, three 152.4 mm diameter cores, and two 101.6 mm diameter cores were obtained for study and testing. Eight of the finished cores (Numbers 7Y, 27W, 31Y, 33Z, 35X, 39X, 51X, and 53Z) were selected for petrologic study by F. B. Nimick (Organization 6313, Sandia National Laboratories) and R. H. Price as representative of the rock as a whole. Letters assigned to the samples refer to depths of core samples, W being closest to face AE, Z being farthest from that surface. Four of the cores (27X, 31Z, 35Z, and 51Z) include two samples from different depths in the same core. The remaining 50 cores included in this study were used for mechanical and physical testing. The mechanical test samples then were cut and machined to right-circular cylinders with tolerances of ± 0.25 mm on the diameter. The samples had nominal finished diameters of 50.8 mm and a nominal length-to-diameter ratio of 2:1.

Macroscopically, samples from the welded, devitrified zone consist of two main components. The majority of the rock consists of a fine-grained matrix identifiable by its dark, generally purple or reddish-brown color. Gray regions of vapor-phase-altered material vary in size and are quite common. In addition, many of the samples contain small (open and closed) lithophysae (Price et al., 1985) and 'healed' (i.e., quartz- or calcite-filled) fractures. All of the rock specimens were described by F. B. Nimick prior to mechanical testing. These brief descriptions are presented in Table 2.

PETROLOGIC PROPERTIES

The mineralogy and petrology of eleven core samples (Numbers 7Y, 27W, 27X, 31Y, 31Z, 33Z, 35Z, 39X, 51X, 51Z, and 53W) of welded tuff were studied in support of the rock mechanics tests, primarily to address two questions. First, are there any significant mineralogic or textural variations between samples that might be reflected in mechanical test results? Second, are there any mineralogic differences between these surface samples and equivalent horizons present beneath Yucca Mountain as sampled in drill holes? In addition to addressing these specific questions, data gathered in the course of this study are presented here to add to the NNWSI Project data base for tuffs from Yucca Mountain and vicinity.

All mineralogy and petrology test sheets and data are on file in Department 6310, Sandia National Laboratories, Data Records Management System (DRMS) data file L04.A - 02/13/84.

Petrography

Welding: All samples studied are moderately to densely welded, based on microscopy and on the following criteria presented by Carroll, Caporuscio, and Bish (1981). Shards show strong deformation around phenocrysts and rigid lithic fragments, and the welded fabric is defined by a notable preferred orientation of shards as well as flattening of relatively rare pumice fragments to form fiamme.

Apical angles of tricuspidate shards deformed during welding may be used to estimate compaction strain (Sheridan and Ragan, 1976). Between 8 and 15 measurements were made per section, except in samples 51X and 51Z in which fine mosaic crystallization destroyed most shard forms. Most shards measured have acute apical angles within the plane of welding. The average acute apical angle from 108 measurements in 11 thin sections cut perpendicular to the welding fabric is 44° , and averages for individual sections range between 35° and 52° . Strain calculations assume that apical angles originally averaged 120° and that welding occurs by uniaxial compression in which the principal strain axis lies perpendicular to the welding fabric. Although these assumptions may not be strictly correct (i.e., some flow in addition to pore reduction may occur during welding), and the method only estimates strain resulting during that phase of welding in which shards are deforming, results should be comparable between samples. Calculations indicate a linear compaction strain of about 30% during welding.

Sheridan and Ragan (1976) suggest that shard deformation occurs during the change from partial welding (density: 1.35 g/cm^3) to dense welding (density: 2.20 g/cm^3) which reflects a 39% reduction in thickness, based on modeling the welding process as pore

space reduction under uniaxial compression. The dry bulk densities of welded Topopah Spring Member matrix from Rock #10 average about 2.25 g/cm³ (B. M. Schwartz, oral comm., 1985), similar to that of densely welded tuff given by Sheridan and Ragan (1976). The calculated 30% reduction in thickness, when combined with the presence of abundant coarse pore-filling quartz (density: 2.65 g/cm³) and feldspar (density: 2.58 g/cm³), suggest that the bulk density is partly related to the presence of these high-density phases and is not strictly the result of welding.

Welding textures in the Rock #10 samples are similar to those described by Vaniman et al. (1984) in USW GU-3 and observed by us in a sample from 261.2 m (857.1 ft) depth in USW GU-3. Samples from an equivalent stratigraphic intervals in USW G-1 and USW G-4 farther north (Figure 1) within Yucca Mountain examined by us are more densely welded.

Crystallization: All samples from Rock #10 are completely devitrified. For descriptive purposes, crystallization textures may be grouped into four textural types. These are discussed in order of increasing crystal size. Predominant in the matrix of most samples is a microcrystalline (replacing very fine 'dusty' nonshard glass) to axiolitic (replacing shards) texture in which crystallization does not cross original fragment boundaries. The second type is a spherulitic texture that overprints shard/dust boundaries, but it is otherwise similar to the axiolitic texture. This type is commonly developed in regions where one would expect anomalous strain, such as locations where welding textures are deflected around rigid phenocrysts and lithic fragments. X-ray diffraction (XRD) indicates the presence of quartz, several feldspar phases, and minor cristobalite in both textural types; the average crystal size is generally less than 2 μ m, and mineral phases are tightly intergrown. Axioitic and spherulitic matrices are typically reddish-brown in color, attributed to finely disseminated iron oxide, probably hematite.

Locally within most samples, the very finely crystalline textures grade into the third crystalline type, a fine mosaic texture in which the intergrown microcrystalline to spherulitic aggregates of feldspar, quartz and cristobalite are recrystallized to a fine equigranular mosaic of the same mineral phases. Individual crystals typically range between 10 and 50 μ m in size in these areas, overprinting and destroying relict shard textures. This fine mosaic texture is dominant in samples 51X and 51Z. XRD results for 51Z suggest that cristobalite is probably more abundant in this material than in the finer-grained devitrified material. In general, this material shows less of the reddish-brown color that dominates the two finer crystallization types, probably due to the crystallization of iron oxides into discrete granular phases, which are visible in thin section.

The fourth textural type is much coarser and corresponds to the granophyric texture of Vaniman et al. (1984). It is typically a coarse, interlocking mosaic of alkali feldspar and quartz that lines the inner surfaces of larger pores and generally shows a coarser filling of the interior of the pores with quartz. Individual crystal sizes are larger than those in the fine mosaic texture, averaging 50-100 μm . With a very few exceptions, granophyric texture is restricted to fiamme, soft gray porous material similar to the vapor-phase altered regions around lithophysae (Price et al., 1985), and very porous lithic fragments. XRD analysis of the soft gray material from sample 51Z indicates that cristobalite is present in a significantly greater amount than in finer matrix types; about 40% of the silica phase is probably cristobalite, in contrast to about 10% for the other types. Although texturally similar to tridymite-rich vapor-phase altered material in the overlying lithophysal tuff (Price et al., 1985), no tridymite was identified in these nonlithophysal samples either optically or by XRD. Based on the clear association of granophyric crystallization with fiamme and gray, altered regions, it is apparent that this type of coarse crystallization is characteristic of the pumice, lithophysae, and altered regions described by F. B. Nimick in the mechanical test samples (Table 2).

Some very minor microcrystalline calcite is present, chiefly in fractures, and is texturally identical to more abundant caliche-type material present in lithophysal cavities in the overlying tuff (Price et al., 1985). Although some vein-type calcite has been reported in USW GU-3 by Vaniman et al. (1984), no surface-deposited material such as that found in the Rock #10 samples is likely to be present at depth within Yucca Mountain.

In the overlying lithophysae-rich horizon within the Topopah Spring Member, previously studied by Price et al. (1985), cristobalite is the dominant silica phase in the devitrified matrix, and abundant tridymite is present as vapor-deposited material in and adjacent to lithophysae. The rarity of these low-density phases in the nonlithophysal tuff studied here is probably the chief reason for the higher grain density in the nonlithophysal samples (average: 2.60 g/cm³) compared to the lithophysal tuff (average: 2.49 g/cm³).

The fine microcrystalline to axiolitic textures and the relatively fine granophyric textures in the Rock #10 samples are very similar to those observed in the USW GU-3 sample from 261.2 m (857.1 ft) depth. The main difference is slightly more extensive vapor-phase crystallization in the latter. Crystallization textures are very similar to those described by Vaniman et al. (1984) for the moderately to densely welded interval between 207 m (608 ft) and 275 m (903 ft) depth in USW GU-3. Our examination of thin sections from equivalent intervals in USW G-1 and USW G-4 (Figure 1) suggests that development of coarser granophyric and vapor-phase crystallization in the matrix is more prominent than in Rock #10 samples.

Porosity: Examination of thin sections suggest that porosity in all types of devitrified matrix is low. Scanning electron microscope (SEM) photographs of epoxy-impregnated, polished, thin sections indicate that most pores are less than $2\ \mu\text{m}$ across, and that the porosity is evenly distributed throughout the rock. Larger pores ($10\text{-}500\ \mu\text{m}$ across) tend to be present in areas of coarse pore-filling granophyric crystallization both as a result of incomplete filling of the pores and the development of intercrystalline pores. Although some larger pores are present in fine-mosaic textured areas, pore size tends to be similar to that in more finely crystalline matrix. SEM images suggest that pores less than $2\ \mu\text{m}$ in diameter probably make up from 10 to 12% of sample volume, and that larger pores make up the remainder of the porosity (probably $<2\%$). Measured porosity averages 13.6% and ranges between 10 and 20% (B. M. Schwartz, oral comm., 1985). Porosities were calculated from measured dry bulk densities and measured grain densities as described in Appendix C of Price et al. (1985). Porosity in a core (52X) adjacent to the samples containing abundant fine mosaic crystallization (51X and 51Z) is 13.0%, close to the average for all samples. This suggests that bulk porosity is not significantly different in these samples, although there may be a slight difference in pore size distribution.

In several samples, quartz-filled (healed) fractures are paralleled by coarsely crystalline zones 0.3-1.0 mm wide in the adjacent matrix, and SEM images show a dramatic increase in porosity to about 20-25% in the $2\text{-}10\ \mu\text{m}$ range in these altered zones. These crystalline zones are texturally intermediate between fine mosaic and granophyric crystallization. The zones and the quartz fill appear to have developed at high temperature during cooling.

Granophyric crystallization should result in the creation of larger pores at the expense of smaller ones because of larger crystal size, and it has been suggested that there should be an inverse relation between crystal size and strength (e.g., Brace, 1964; Olsson, 1974; Hugman and Friedman, 1978). Coarse vapor-phase alteration and granophyric crystallization appear to correlate positively with porosity. The average porosity measured on Rock #10 samples is $13.6\pm 2.7\%$ (F. B. Nimick, oral comm., 1986). Porosity measured in the texturally similar USW GU-3 261.2 m (857.1 ft) sample is 12.3%, and measured porosities on three USW G-4 samples from a stratigraphically equivalent interval range between 9.8 and 13.7% (F. B. Nimick, oral comm., 1986). Petrographic examination of these samples suggests that the higher porosity values within individual samples of devitrified tuff from USW G-4 are associated with a greater abundance of zones of coarse, vapor-phase, and granophyric crystallization, and that small variation in porosity (between about 9 and 14%) are not well-correlated with the variation in degree of welding indicated by shard deformation and flattening textures.

Matrix Mineralogy and Composition

Defocussed-beam electron microprobe analyses of devitrified matrix were made to determine the composition of the material that forms the bulk of the rock. These data, in combination with identification of mineral phases present in the matrix by XRD, have been used semiquantitatively to determine the mineralogical make-up of the matrix. Analyses of the different textural varieties of matrix (microcrystalline axiolytic, spherulitic, and fine mosaic) were made to determine what, if any, chemical variation occurs among these varieties.

All analyses of microcrystalline and axiolytic matrix and finely crystalline spherulites associated with shard-rich areas indicate a high-silica rhyolite composition with SiO_2 generally greater than 76 wt% (Table A-1; i.e., the first table in Appendix A). Molecular amounts of Na_2O exceed K_2O so that Na/K ratios range from 1.02 to 1.65 and average 1.24. Figure 3 is a ternary plot of Na_2O , K_2O and CaO as molecular end members. Molecular norms calculated from the analyses (Table A-1) consist of 33 to 46% (average 38%) quartz (including all silica phases), 21 to 32% (average 29%) orthoclase, and 28 to 38% (average 32%) albite. Anorthite is generally about 1% and mafic minerals (chiefly iron/titanium oxides, hypersthene, and enstatite) invariably compose less than 3% of the norm. There is no notable difference in major element composition between spherulitic, microcrystalline, and axiolytic matrix.

Analyses of reddish-brown microcrystalline, axiolytic, and spherulitic matrix typically contain two to three times as much iron (arbitrarily reported by the microprobe as FeO) than does clear areas of matrix with similar texture (Table A-1, Analyses 2, 3, 15, and 16). This indicates that the reddish-brown color is the result of the presence of finely disseminated iron oxide (probably as hematite, Fe_2O_3). Except for the iron content, there is no notable difference in major element chemistry that could suggest the presence of clays or other minerals related to this color difference.

XRD analysis of microcrystalline/axiolytic and spherulitic matrix indicates that quartz and two or three alkali feldspars are present. Cristobalite may be present, but very low peak intensity suggests that it is under 5%, and no tridymite is evident. XRD analyses of fine mosaic matrix show slightly more cristobalite, but are otherwise indistinguishable from analyses of more finely crystalline material.

Coarsely crystallized granophyric matrix in pores and fiamme is generally more variable in composition and contains optically distinct larger feldspar and quartz (up to $50\ \mu\text{m}$ across), which makes reliable determination of average composition by microprobe difficult. The abundance of quartz suggests that granophyric matrix is more silicic than more finely crystalline types, and this is supported by high silica contents in the microprobe analyses and relatively high quartz (average 45%) in the molecular

norms (Table A-1, Analysis 13; Table A-2, Analyses 1 and 3). XRD analyses suggest that quartz and cristobalite are present in subequal amounts in some granophyric areas in fiamme, but optical examination indicates that the granophyric material that crystallized in pores in the matrix is strongly dominated by quartz. No tridymite is evident. The same two or three feldspars identified in the microcrystalline matrix are present in the granophyric matrix. Microprobe analyses (Table A-3) indicate that sanidine (average $An_1Ab_{40}Or_{59}$) is dominant, but subordinate sodic sanidine ($An_3Ab_{54}Or_{43}$) is also present locally.

Nongranophyric areas in fiamme are typically dominated by spherulitic crystallization, in contrast to the relatively rare spherulites in the shard matrix. Microprobe analyses indicate two distinct fiamme compositions. One is very similar to shard matrix except for slightly lower Na/K ratios (Table A-2, Analyses 1, 3, 4, and 5). The second is less common, tends to be strongly reddish brown in color, is low in SiO_2 (typically under 70 wt%), and very potassic and Al-rich (Table A-2, Analyses 2 and 6). Compositionally these are quartz latites, similar to the caprock of the Topopah Spring Member except for the high potassium content.

Samples 51X and 51Z contain a relatively larger proportion of fine mosaic crystallization in the matrix than other samples. Although low analytical totals in some analyses suggest that an increase in porosity may be related to this crystallization, chemical differences between analyses are minor (Table A-1, Analyses 12, 13, and 14).

Several spherulitically crystallized lithic fragments were analyzed, and all are very silicic, with about 80 wt% SiO_2 . All are microporphyritic and probably of volcanic origin.

Feldspar Phenocrysts: Plagioclase (Table A-4) and sanidine (Table A-5) are present as phenocrysts in all samples. Plagioclase is approximately twice as abundant as sanidine and is mostly oligoclase ($An_{17}Ab_{78.5}Or_{8.5}$), although plagioclase ranging up to andesine (An_{48}) is also present (Figure 4). The more calcic varieties tend to occur as distinct cores, mantled by sanidine or plagioclase of more typical composition. Sanidine shows less compositional variation than plagioclase, and the analyses (Table A-5; Figure 4) tend to fall into two groups of very similar composition, $An_2Ab_{45}Or_{53}$ and $An_2Ab_{40}Or_{58}$. Center to edge zoning traverses in feldspars indicate that phenocrysts of the dominant composition are essentially unzoned. Although some weak oscillatory zoning is evident in more calcic plagioclase cores, feldspar overgrowths of more typical composition are unzoned. Most sanidine phenocrysts show a compositionally distinctive (but optically obscure) alteration rim, 20-30 μm thick, in which Ab increases slightly at the expense of Or. Oligoclase shows a similar but less consistent increase in Ab at the expense of Or and/or An in the rim. This marginal alteration presumably occurred during devitrification.

The two-feldspar graphical geothermometer of Brown and Parsons (1981), when applied to the dominant compositions (excluding the altered rims), suggests magmatic equilibration at 700-720°C at an assumed pressure of 100 MPa. Although there is considerable uncertainty regarding the precision of the geothermometer (see Brown and Parsons, 1981; Stormer and Whitney, 1985), comparison of feldspar temperatures throughout the Topopah Spring Member may yield some instructive information on relative temperature gradients in the magma chamber. The temperatures for these samples are somewhat lower than those obtained utilizing iron-titanium oxide geothermometry; the pressure dependence of the feldspar geothermometer suggests that the pressure in the magma chamber may have been higher than the assumed 100 MPa (Stormer and Whitney, 1985). Reaction kinetics for feldspars are extremely sluggish (Brown and Parsons, 1981), and the similarity of iron-titanium oxide and feldspar temperatures strongly suggest that *in situ* reequilibration did not occur.

Biotite Phenocrysts: Biotites from three of the cores were analyzed and are very homogeneous with respect to most elements, except for variations in magnesium, iron and manganese (Table A-6). Molecular Mg/(Mg+Fe) ratios in biotite tend to be consistent throughout eruptive units at the NTS (Warren, Byers, and Caporuscio, 1984) and are useful in correlating drill hole samples where physical correlation is difficult because of textural variations. Broxton et al. (1985) have indicated that Mg/(Mg+Fe) ratios in biotites from the lower part of the Topopah Spring Member are generally between 0.35 and 0.45, and those from the upper part are generally between 0.55 and 0.65. All but one biotite from these nonlithophysal samples (Table A-6) fall into the low magnesium range, whereas biotites from the immediately overlying upper lithophysal zone have ratios in the high magnesium range (Price et al., 1985). The sharp contrast in biotite composition suggests a change in magma composition across this boundary and adds further evidence to the suggestion by Scott et al. (1983) that the lithophysal zone is a stratigraphic unit within the Topopah Spring Member.

Iron-Titanium Oxides: Magnetite and ilmenite are ubiquitous minor phases in all samples. Exsolution of a Ti-rich ilmenite from magnetite and Ti-poor magnetite from ilmenite is characteristic of slow cooling. The presence of homogeneous magnetite and ilmenite imply either quenching from magmatic conditions or *in situ* reequilibration at high temperature. Partition of Fe and Ti between homogeneous ilmenite and magnetite has been shown to be a sensitive indicator of temperature (T) and oxygen fugacity (fO_2), and much recent work has refined the application of such a geothermometer (Spencer and Lindsley, 1981; Stormer, 1983).

Of the two samples in which ilmenite and magnetite were analyzed, only one (33Z) contains unexsolved magnetite and ilmenite phenocrysts, which give good analytical totals when iron is partitioned stoichiometrically into FeO and Fe₂O₃ (Table A-7). T and fO_2 values were calculated for all combinations of magnetite and ilmenite with

recalculated totals greater than 97.5%. Recalculation of analyses, based on various schemes for partitioning minor elements and calculation of T and f_{O_2} , was accomplished by use of a computer program written by Stormer (1983). Results are shown in Figure 5. The range in temperatures calculated is 730 to 790°C, and the range in oxygen fugacity is $10^{-14.5}$ to $10^{-13.5}$ atm. The magnetite displaying some exsolution (O_5) yields the highest temperatures, and is probably not indicative of equilibrium conditions. The T- f_{O_2} results suggest conditions slightly more oxidizing than the nickel/nickel oxide (N/NO) buffer. It should be noted that, of the ilmenites used, O_2 is extremely rich in manganese (MnO), resulting in a large difference in calculated mole fraction of ilmenite (XILM) depending on the recalculation procedure used; the variation in calculated temperatures, however, is relatively small, generally not more than 15°C.

Feldspar temperatures, if valid, must represent magmatic conditions because equilibration of feldspars outside the magmatic environment is extremely unlikely (Brown and Parsons, 1981). The fairly close agreement of oxide temperatures with temperatures derived from feldspar thermometry suggests that either the oxides did not reequilibrate during devitrification or that emplacement and devitrification temperatures were not significantly lower than those in the magma.

Comparison with Yucca Mountain Drill Hole Samples: Plagioclase and alkali feldspar phenocrysts in two samples of devitrified tuff from the same stratigraphic interval as Rock #10 in USW G-1 (depths of 329.0 and 368.4 m; 1079.4 and 1208.7 ft) are identical in composition (within the limits of analytical error) to those reported here from Busted Butte. They are notably different from phenocrysts in the overlying upper lithophysal zone analyzed previously (Price et al., 1985). As discussed earlier, the USW G-1 samples are considerably different from the Rock #10 samples in both welding and crystallization textures. These textural variations can probably be attributed to emplacement of the USW G-1 (and USW G-4) samples in a thicker pile closer to the source, which has resulted in more dense welding and more extensive late-stage crystallization resulting from the effects of trapped fluids and gases.

Estimation of Grain Densities from Mineralogical Data

As an independent check on grain density measurements obtained by B. M. Schwartz (oral comm., 1985) on the matrix of Rock #10, grain densities were estimated using molecular norms calculated from microprobe analyses of matrix areas and results of XRD analysis. The calculations assume the following:

1. Molecular norms approximate modal (volume) percentages of minerals present.
2. Normative 'quartz' includes both quartz (density: 2.65 g/cm³) and cristobalite (density: 2.33 g/cm³). XRD data suggest that, in the devitrified matrix, nor-

native 'quartz' is about 90% quartz and 10% cristobalite, and, in fiamme and granophyric areas, normative 'quartz' is about 60-70% quartz and 30-40% cristobalite.

3. Normative feldspar (albite + orthoclase + anorthite) may be modeled as a single sanidine phase with a density of 2.58 g/cm^3 . Although XRD data imply that subsolidus exsolution of feldspar has occurred, this should not affect density significantly.
4. The remaining mafic constituents range between 1 and 3% and are assumed to consist of equal amounts of hematite (density : 5.20 g/cm^3) and biotite (3.86 g/cm^3).
5. Any corundum in the norm is assumed to represent smectite clay with density of 2.5 g/cm^3 .

Given these assumptions, calculated grain densities for microcrystalline to axiolitic and finely spherulitic (devitrified) matrix are between 2.61 and 2.63 g/cm^3 . Assuming that all mafics are hematite, the density would increase by 0.02 - 0.03 g/cm^3 ; this range of 2.63 - 2.65 g/cm^3 may be considered an upper limit because the actual hematite present is probably less dense than the assumed value for nonhydrated specularite.

In rhyolitic, spherulitic fiamme and granophyric matrix, the assumed higher cristobalite content generally reduces calculated grain densities to between 2.57 and 2.60 g/cm^3 . In quartz latitic (lower SiO_2) fiamme, calculated grain densities are typically about 2.60 g/cm^3 . The lowest calculated grain density is 2.57 g/cm^3 for a corundum-normative, silica-rich fiamma in 51X, in which 30% of the silica phase is assumed to be cristobalite and the corundum is assumed to be smectite.

Measured grain densities for Rock #10 samples range from 2.56 to 2.67 g/cm^3 , averaging 2.62 g/cm^3 for one suite of samples and 2.60 g/cm^3 for another (B. M. Schwartz, oral comm., 1985). Agreement between measured and calculated values is very good, with calculated values averaging slightly higher (typically by 0.02 g/cm^3) than measured values. Given the uncertainties involved in both the calculated and measured results, and explanation of this variation is not warranted. The close agreement suggests that the calculated norms approximate the actual mineralogy of the devitrified matrix.

MECHANICAL PROPERTIES

This section presents the results of deformation experiments on 44 oven-dried and vacuum-saturated samples. The tests were performed in compression at effective confining pressures of 0, 5, and 10 MPa; temperatures of 22 and 150°C; and nominal axial strain rates of 10^{-7} , 10^{-5} , and 10^{-3} s^{-1} . Previous mechanical tests conducted on intact samples of the Topopah Spring Member of the Paintbrush Tuff have been reported by Olsson and Jones, 1980; Price, Nimick and Zirzow, 1982; Price, Spence and Jones, 1984; Price et al., 1985; Nimick et al., 1985; Price, 1986; and Nimick, VanBuskirk, and MacFarland, in preparation.

All mechanical property calibration records, saturation and drying records, test sheets, and test results can be found in one of the following Department 6310, Sandia National Laboratories, DRMS data sets: L02A1.A - 08/04/83, L02A1.A - 12/05/84, or L02A1.A - 06/26/85.

Experimental Techniques

Each of the mechanical experiments presented here was performed on one of three load frames. The capacities of the three frames are 0.9, 1.8, and 4.9 MN. In each case, a constant displacement rate of the loading piston was achieved by servo-control of the hydraulic loading ram while monitoring a linear variable displacement transformer (LVDT) connected to the loading column.

A discussion of the calibrations of the load cell, axial and lateral displacement gages, and the test system calibration checks are presented in Appendix B.

Throughout this test series, confining pressure, P_c , and pore pressure, P_p , were measured with standard pressure gages. Effective pressure, P_e , was then calculated from these values (i.e., $P_e = P_c - P_p$). The pore pressure was not measured for the tests run at room temperature. These tests were run drained (i.e., the pore fluids were allowed to vent through a hole in one of the end caps), and the pore pressure in these experiments was always assumed to be atmospheric (or about 0.1 MPa). Differential stress, $\Delta\sigma (= \sigma_1 - \sigma_2)$, was calculated by dividing the post-hydrostatic loading force (i.e., the increment of force above that resulting from the confining pressure), measured on a standard load cell, by the original cross-sectional area of the sample. Axial strain, ϵ_{ax} , was calculated by one of two methods, (1.) averaging the measured displacements on two diametrically opposed LVDTs mounted directly on the sample and dividing by the average value of the original gage lengths or (2.) dividing the measured displacement on the control LVDT (minus machine and end-cap displacements) by the original sample length. Lateral (transverse) displacement was measured across one sample diameter (located in the middle of the sample) by a ring gage (Holcomb and McNamee,

1984). Lateral strain, ϵ_{lat} , was then obtained by dividing the lateral displacement by the original diameter of the test specimen. Volumetric strain, ϵ_v , was calculated by summing the three principle strains (i.e., $\epsilon_v \approx \epsilon_1 + \epsilon_2 + \epsilon_3 \approx \epsilon_{ax} + 2\epsilon_{lat}$). Axial force, axial displacement, lateral displacement, and time data were collected and reduced on a *DEC (Digital Equipment Corporation) LSI 11/23* computer, with software described by Holcomb and Jones (1983). The data were subsequently transferred to a *DEC VAX 11/780* for plotting, using *GRAPH III (Selleck, 1986)*, and analysis.

For tests run at elevated pressures, a bulk modulus, K , was calculated as the slope of a linear regression fit to the hydrostatic pressure-volumetric strain data. Young's modulus, E , and Poisson's ratio, ν , were determined from the slopes of the linear regression fits to the differential stress-axial strain and lateral strain-axial strain data, respectively. In both of these cases, the fits were obtained using only those data corresponding to stress states from 10 to 50% of the ultimate strength of the particular test sample. The ultimate differential stress value, $\Delta\sigma_u$, is the peak value of differential stress the sample withstood under the stated experimental conditions. The axial strain at ultimate stress, $(\epsilon_{ax})_u$, corresponds to the magnitude of sample axial strain at the peak stress.

After machining, all test samples were stored in distilled water and/or groundwater from Well J-13 (NTS). Depending on the defined experimental conditions, the samples were treated in one of two ways before testing. The samples to be tested dry were placed in an oven and heated to 105°C for at least 120 hours, cooled in the oven, and then weighed. They were then subjected to as many additional drying cycles as were necessary to meet the criterion (listed below) for a dry sample. These additional drying cycles included heating to 105°C for 24-36 hours followed by cooling and weighing of the samples. The samples to be tested saturated were submerged in water and subjected to 3 or more saturation cycles that included at least 18 hours under an active vacuum (≤ 600 Pa) followed by submersion for 6 hours at ambient pressure. After each saturation stage the samples were weighed. The samples were considered to be saturated (dry) when the weight gain (loss) after a given saturation (drying) step was less than or equal to 0.05% of the weight at the beginning of the step. After these preparations, and before mechanical testing, the dry samples were kept in an air-tight container with desiccant, and the saturated samples remained submerged.

In preparation for mechanical testing, samples to be tested at elevated pressure were jacketed in polyolefin shrink-tubing and sealed to the diameter-matched end caps. For tests at elevated temperature, samples were jacketed in flexible viton tubes and sealed to the end pieces. In each case, the axial and transverse transducers then were mounted on the sample and the sample assembly was placed in the loading column. At this stage, the unconfined, room temperature experiments were begun. However, for all of the confined tests, the confining pressure was raised and allowed to equilibrate prior to testing. The

saturated samples tested at elevated temperatures were initially subjected to confining and pore pressures of about 2 MPa (in all cases, an effective pressure of approximately 0.2 MPa was maintained to preserve the integrity of the jacket so that water was not allowed to invade the silicon oil confining pressure system). These confining and pore pressures were necessary to ensure that the water in the sample would remain in a liquid state at 150°C. The temperature was raised slowly (~1°C/min) and allowed to equilibrate, at which time the test was begun for the effectively unconfined experiments, or the confining pressure was raised to produce the desired effective pressure level before testing.

Experimental Results

A summary of the bulk and Young's moduli, Poisson's ratio, ultimate strength, and axial strain at failure results is given in Table 3. In addition, the means and standard deviations of the mechanical property data, for each set of experimental conditions, are listed in Table 4.

The differential stress/axial strain curves for all mechanical tests are presented in Figures 6a-k. The general shapes of the differential loading curves presented here are very similar to results reported for previous tests on other samples of densely welded, silicic tuff from the Topopah Spring Member (e.g., Price, Spence, and Jones, 1984; Nimick, et al., 1985).

A discussion of the mechanical property results must be prefaced by the cognizant understanding that only three or four samples were deformed at most of the defined sets of experimental conditions. In addition, there is a wide diversity in petrofabric features (e.g., pumice, alteration, lithophysae, and fractures) within these tuffaceous rocks (see Table 2) and previous mechanical property data from tests on tuff samples have consistently exhibited a large inherent scatter (e.g., Price and Bauer, 1985; Price, 1986). Together, these facts indicate that any conclusions made from these data must be considered to be preliminary. Additional tests on samples from the same outcrop, at the same sets of conditions, are needed to increase the data base, and therefore to increase the confidence in or to redefine the conclusions. There are, however, some important conclusions made during this study, especially when relating the mechanical property results to the detailed petrologic/mineralogic characterizations of this rock and brief physical descriptions of the mechanical test samples.

When reviewing the general test results in the following paragraphs, each discussion will be preceded by a subsection heading including the number of samples tested and the experimental conditions used for these samples. The information is presented in the following format:

number of samples, saturation, pressure, temperature, strain rate:

Four Samples, Dry, 0 MPa, 22°C, 10^{-5}s^{-1} : The differential-stress loading curves for these samples are presented in Figure 6a. The pre- (Table 2) and post-test sample examinations have shown that the preexisting open fracture and highly porous, altered areas dominated the deformation of sample 41Y and the high-porosity altered area dominated the deformation of sample 46W, and, as a result, these samples had very low strengths (see Table 3a). In addition, the chipped ends of 41Y probably contributed to a premature failure, because several fractures intersect these areas of stress concentration. The comparatively low Young's modulus of 34Z appears to be the result of a large volume of relatively high porosity pumice and altered material within this sample. The effect of these petrofabric features on Young's modulus was accentuated by their long axes being oriented almost perpendicular to the sample axis. This is the type of petrofabric variability responsible for the large scatter in the mechanical data of tuffs.

Four Samples, Dry, 0 MPa, 22°C, 10^{-7}s^{-1} : Three of the differential stress/axial strain test results (Figure 6b) are very similar, with only minor ranges in the elastic and strength properties. The fourth sample tested, 28X, has relatively low moduli and a strength that was less than half of the other three samples. These differences were probably the result of 28X containing a significant region of altered matrix (Table 2).

Three Samples, Dry, 5 MPa, 22°C, 10^{-5}s^{-1} : The hydrostatic pressure and differential-stress loading (Figure 6c) behaviors are similar for the three samples. This similarity is reflected in the resultant bulk moduli, Young's moduli, Poisson's ratios, and ultimate strengths for the three samples (Tables 3a and 4).

Three Samples, Dry, 10 MPa, 22°C, 10^{-5}s^{-1} : The differential-stress loading curves for these samples (Figure 6d) exhibit two distinctly different characters. Sample 25Z deformed in essentially a linear-elastic fashion, with an abrupt loss of strength at failure. The other two samples (43W and 50Y) were initially elastic, but with a broad yield leading to either no or a minor loss in strength following the sample reaching its ultimate strength. This difference probably results from the absence (in 25Z) or presence (in 43W and 50Y) of relatively large pumice or areas of alteration. These highly porous features tend to collapse, producing a more homogeneous, stable sample deformation (reflected by a stress/strain curve with a broad yielding) instead of one or two fractures unstably propagating through an entire sample quickly (shown by a stress/strain curve that is linear elastic up to failure with a sudden, large loss of load-bearing capability).

Four Samples, Saturated, 0 MPa, 22°C, 10^{-3}s^{-1} : The resulting stress/strain curves for these samples are plotted in Figure 6e. There is a distinct difference in the ultimate strengths observed for two of the samples (23X and 24Y), but this disparity is interpreted to be natural and the result of differing amounts of preexisting inhomogeneities (e.g., small healed fractures, closed lithophysae, small pumice, and lithic

fragments). However, a relatively large volume and/or number of inhomogeneities dominated the mechanical behavior of the other two samples (38X and 52Z). As described in Table 2, these samples contain large, highly porous pumice and altered zones, which acted as local, weakened regions that failed prematurely, producing low ultimate stress values.

Six Samples, Saturated, 0 MPa, 22°C, 10^{-5}s^{-1} : The differential-stress loading curves for these samples are presented in Figure 6f. All six samples behaved essentially linearly elastic up to failure, and the scatter in elastic and strength properties is assumed to be typical for this inhomogeneous material.

Four Samples, Saturated, 0 MPa, 22°C, 10^{-7}s^{-1} : This is another example of three samples (4Y, 44X, and 53Z) behaving in a similar manner and one sample (25Y) being distinctly different (Figure 6g). As noted in Table 2, sample 25Y contained a pre-existing, open fracture oriented at 30° to the sample axis. This sort of anisotropy tends to dominate the deformation of a relatively small-volume (i.e., laboratory-scale) sample. As a result, the determined strength value is not really indicative of the strength of the intact rock, but more reflective of the shear strength of the anisotropy. On the other hand, sample 44X is a prime example of a test specimen being able to contain a relatively large anisotropy with little or no effect on the mechanical response of the rock. When a sub-planar weak zone (in this case a closed lithophysa) occurs within a sample oriented approximately perpendicular to the sample axis, then little or no shear stress is developed on the structural feature. Because σ_1 is essentially a normal stress on the plane, the applied stress works to flatten the discontinuity toward planarity, and therefore, the strength of the anisotropic feature is as great as the strength of the intact rock.

Three Samples, Saturated, 5 MPa, 22°C, 10^{-5}s^{-1} : The differential stress/axial strain curves for these samples are presented in Figure 6h. The elastic properties, strengths, and stress/strain behaviors for these three experiments are very similar.

Six Samples, Saturated, 10 MPa, 22°C, 10^{-5}s^{-1} : Six tests were planned at 10 MPa, but some problems caused one to be run only hydrostatically (10W) and, in another test, only strength data were collected during the differential loading phase (3Z). The four remaining differential stress/axial strain curves appear in Figure 6i. The range of resultant Young's modulus values is narrow, indicating similar initial mechanical response; however, the ultimate strength values vary by almost a factor of 2. Neither the pre-test descriptions (Table 2) nor the post-test examinations of the samples indicated any obvious reasons for the disparity in strengths, so it is assumed that it is the result of natural minor petrologic differences within the samples.

Four Samples, Saturated, 0 MPa, 150°C, 10^{-5}s^{-1} : Figure 6j presents the differential stress/axial strain results for these samples. These curves are all very similar.

The lower yield and ultimate strength of sample 48Y are the result of the presence of two large, highly-porous pumice fragments (Table 2).

One distinction in the plots in Figure 6j from the previously presented results is the initial concave upward trend in all four curves. Undoubtedly, this is not a real difference in the mechanical response of these particular samples, but rather the result of not having an effective method of subtracting the initial nonlinear response of the interfaces in the loading column (axial strain was measured outside of the pressure vessel in all high-temperature tests). In spite of careful machining, polishing, and cleaning of loading platens, end caps, and the rock sample, the interfaces still had very minor misalignments and minute asperities. Until the interfaces are completely closed from a finite amount of normal stress, the resulting load/displacement curve for the loading column is nonlinear, even though, under these stress conditions, each piece is linearly elastic.

The reader will note that no Poisson's ratios appear in Table 3c for the elevated temperature tests. In the the high-temperature testing system, volume strains (and, indirectly, lateral strains) are measured dilatometrically (volumetric change in confining fluid). This system, however, was not operational when these experiments were performed.

Three Samples, Saturated, 5 MPa, 150°C, 10^{-5} s^{-1} : The differential-stress loading curves from these experiments are presented in Figure 6k. Two of the samples (14W and 35Y) were very similar in their mechanical behavior. However, the third sample (34W) was markedly different (i.e., one-half the Young's modulus and one-third the strength). Actually, this behavior is not indicative of tuff, but of the altered material with included pumice fragment (see description of 34W in Table 2). This material is much higher in porosity and much less consolidated, which, expectedly, results in the less competent mechanical behavior. A post-test examination of the sample bears out this assumption. The major through-going fracture extends from the pumice and is entirely contained within the altered zone.

Discussion

In general, a considerable number of inferences can be made from the pre-test hand specimen examinations in regard to mechanical properties. Healed fractures seem to have little or no effect on the elastic and/or strength properties. Sample 3W is a prime example. It contained a relatively large, healed fracture occurring in a very favorable orientation for large shear stresses ($\sim 30^\circ$ to sample axis); however, this sample had a Young's modulus similar to the other samples in the data set and the highest strength among these four test specimens. Usually, open fractures significantly lower sample strength (e.g., 25Y). Also, relatively large volumes of lithophysae, highly porous pumice,

or highly porous, altered material tend to lower both elastic and strength properties (e.g., 28X, 34W, 41Y, 48Y, and 52Z). In addition, in any given sample the test-induced fracture density is invariably much greater (about an order of magnitude) within highly porous pumice or altered zones than within the highly welded, low porosity matrix.

While none of the data in this series has been eliminated from consideration, it must be made clear that some sample deformations were controlled by pre-existing anisotropies and relatively large inhomogeneities (e.g., 25Y, 28X, 34W, 41Y, 48Y, and 52Z). The strengths of these samples (Table 3) are actually more indicative of the strengths of those inherently weak zones than they are of the tuff as a whole. These mechanical test results tend to skew the mean data downward at a given set of experimental conditions. As observed in earlier studies (e.g., Price and Bauer, 1985), the inherent scatter in mechanical properties of tuffaceous rock is quite large; however, Price and Bauer (1985) found a distinct trend in the ultimate strength-functional porosity (defined by Price and Bauer, 1985, as void plus montmorillonite volume percentage) data. They fit this trend with the following empirical power law model:

$$\Delta\sigma_u = 4.04 n^{-1.85}, \quad (1)$$

where $\Delta\sigma_u$ is ultimate stress in MPa and n is functional porosity in volume fraction. Looking only at the best fit strength results from Price and Bauer (1985), if 0.02 (volume fraction) functional porosity is homogeneously added to a rock with an initial functional porosity of 0.10, then the resultant mean strength of the higher porosity material would be only 29% less than the original rock. On the other hand, if that extra 0.02 total porosity were concentrated in pumice and altered regions of relatively high porosity (Price et al., 1985, calculated that these regions have a mean porosity of about 0.50) making up 0.05 of the total sample volume, a realistic approximation from hand specimen examination of the samples listed above, then the decrease in strength would be, in general, much more radical (perhaps a factor of 2). At the other extreme, however, the strengths of samples containing no open fractures, open lithophysae, pumice, or altered zones are not truly indicative of the bulk rock response either and are generally stiffer and stronger than a 'representative' or 'unit' volume of Topopah Spring Member rock (which would have to contain some inhomogeneities).

Saturation Effects: No difference in bulk moduli is observed in the dry and saturated samples run at 5 MPa; however, the mean bulk modulus for the saturated samples was 10% higher than that for the dry samples tested at 10 MPa. When pores in a material are filled with water (an 'incompressible' liquid) instead of air (a highly compressible gas), a larger bulk modulus for the sample as a whole is to be expected. Because there are a few percent of the voids that do not contain water in the 'saturated' samples (even after meeting the saturation criteria), these dry voids are undoubtedly being compressed at the low pressures, and therefore no difference in the bulk moduli of the

'saturated' and dry samples is noted. As the pressure is increased, however, the water begins to be compressed in the saturated samples creating a stiffer system than in the dry samples.

No distinct trends are observed in the Young's modulus and Poisson's ratio data relative to these extreme saturation changes for samples at $P_e = 0, 5$ or 10 MPa and $\dot{\epsilon}_{ax} = 10^{-5} \text{ s}^{-1}$ or at $P_e = 0$ MPa and $\dot{\epsilon}_{ax} = 10^{-7} \text{ s}^{-1}$.

The strength/saturation results are neither consistent nor conclusive. In general, the saturated samples tested under unconfined conditions (and $\dot{\epsilon}_{ax} = 10^{-5} \text{ s}^{-1}$) were actually stronger (a mean increase of 15%) than the dry samples. This is the opposite effect found in most mechanical property studies on silicic rocks and previously noted specifically for Nevada tuffs (Olsson and Jones, 1980; Price and Jones, 1982). The results from saturated and dry samples tested at 5 MPa, 10 MPa, and 10^{-7} s^{-1} exhibit the expected trend (saturated-to-dry strength increases of 7, 40, and 15%, respectively).

Pressure Effects: There is a consistent direct relationship between bulk modulus and effective pressure for both the saturated and dry test samples. The average bulk modulus for saturated samples tested at 10 MPa effective confining pressure was 46% higher than that for samples tested at 5 MPa. The increase was 32% for dry samples over the same effective pressure range. This trend is undoubtedly the result of pumice and altered areas being crushed at low pressures, with the tuffs beginning to stiffen at higher pressures as the porosity becomes significantly compacted. Somewhat counter to this, however, is the inverse relationship of Young's modulus and effective pressure for dry samples at room temperature, saturated samples tested at room temperature, and for saturated samples tested at 150°C. In each case, the average decrease in Young's modulus is about 7% per 5 MPa increase in effective pressure.

The ultimate strength ($\Delta\sigma_u$) versus effective confining pressure (P_e) experimental data were fit by linear regression and then transformed into shear stress (τ)/normal stress (σ_n) space for calculation of the Coulomb failure criterion values in the same manner as described by Olsson and Jones (1980). The Coulomb equation is as follows:

$$\tau = \tau_0 + \sigma_n(\tan \phi), \quad (2)$$

where τ is shear stress, τ_0 is cohesion, σ_n is normal stress, and ϕ is the angle of internal friction. The τ_0 and ϕ values for the three sets of experimental conditions are listed in Table 5. These results are inconclusive because of small data sets, data scatter, and the low correlation coefficients obtained in the $\Delta\sigma_u/P_e$ fits. However, these τ_0 and ϕ data do fit within the ranges of these parameters for Yucca Mountain silicic tuffs reported by Price (1983, Figures 16 and 17).

Temperature Effects: In general, Young's modulus decreases with increasing temperature from 22 to 150°C. Effectively unconfined samples at the elevated temperature

had, on average, 16% lower moduli than the room temperature samples. There is more of an effect at $P_e = 5$ MPa (21%) if the anomalously weak, compliant sample 34W is considered, but only a slight effect (4%) if 34W is ignored.

A mean ultimate strength decrease of 16% resulted from increasing the temperature from 22 to 150°C at both 0 and 5 MPa effective pressure. When sample 34W is taken into consideration, the decrease in ultimate strength was 35% at $P_e = 5$ MPa.

Strain Rate Effects: Almost all studies of the effects of strain (or stress) rate on rock have shown that Young's modulus is directly related to rate. Contrary to this, the saturated samples deformed in this study at room temperature and pressure conditions and axial strain rates of 10^{-7} , 10^{-5} , and 10^{-3} s^{-1} exhibited an average decrease in Young's modulus of 7% per decade increase in strain rate. The dry samples tested at unconfined, room temperature conditions showed a slight, but expected trend. The mean Young's modulus decreased 6% with the two orders of magnitude decrease in strain rate from 10^{-5} to 10^{-7} s^{-1} .

A general increase in ultimate strength with decreasing strain rate is observed in both the dry (11% strength increase per decade decrease in strain rate) and saturated (4% per decade) data. These trends are the opposite of published results on most rock types, including NTS tuffs (Olsson and Jones, 1980; Price and Nimick, 1982; Price and Jones, 1982; Price, Nimick, and Zirzow, 1982; Nimick et al., 1985; Nimick, VanBuskirk, and MacFarland, in prep.).

Summary: To reemphasize, each of the above discussion areas should be concluded by the reminder to note the small number of tests in each data set and the large standard deviations for most of the properties reported in Table 4. The conclusions drawn from these data must, therefore, be carefully examined before being used in any definitive modeling effort.

In addition, it is apparent from this data set that petrofabric variability in the tuff samples is a greater factor affecting laboratory mechanical properties of 50 mm diameter samples than is the variation of the environmental parameters such as saturation, pressure, temperature, and strain rate over the ranges of these parameters expected within a Topopah Spring Member repository within Yucca Mountain.

CONCLUSIONS

Phenocryst and matrix compositions determined by XRD and electron microprobe analyses indicate no significant compositional differences between the 11 core samples analyzed from Rock #10. All samples are completely devitrified to a mixture of feldspar and quartz with minor cristobalite and hematite. Quartz is the dominant silica phase in these samples. While the samples analyzed from Rock #10 are compositionally and mineralogically homogeneous, there are notable textural variations resulting from inhomogeneous distribution of various types of matrix, fiamme (pumice), alteration (granophyric and vapor-phase), and fractures in individual samples. These variations are also evident in the samples used for mechanical and physical property tests (see Table 2).

In terms of composition of feldspar and biotite phenocrysts, the Rock #10 samples are indistinguishable from stratigraphically equivalent horizons in drill holes within the Yucca Mountain repository block. The Rock #10 samples are texturally similar to stratigraphically equivalent samples from USW GU-3, which is the southern-most continuously cored exploratory hole at Yucca Mountain. Samples from the same horizon in USW G-1 and USW G-4, located further north, show denser welding and, in general, more extensive and uniformly distributed coarse granophyric crystallization than either Rock #10 or USW GU-3 samples, probably because of emplacement in a thicker pile closer to the source caldera north of Yucca Mountain as located by Byers et al. (1976). Coarse granophyric crystallization in the Rock #10 samples is largely restricted to fiamme (pumice) and discrete regions of alteration.

In marked contrast to the Rock #10 samples, the dominant silica phases in the overlying lithophysal tuff are cristobalite and tridymite (Price et al., 1985). This difference results in calculated and measured grain densities for Rock #10 which are significantly higher than those of the lithophysal tuff. In addition to obvious variations in texture and silica phases present, there are notable differences in biotite and feldspar phenocryst compositions between Rock #10 and the overlying lithophysal tuff (Price et al., 1985) that suggest that there is a distinctive stratigraphic break between the upper lithophysal zone and the underlying nonlithophysal tuff. Similar breaks in drill hole samples suggest that this is consistent throughout Yucca Mountain.

Petrographic study of Rock #10 samples and a limited suite of samples from Yucca Mountain drill holes for which thin sections and porosity measurements are available suggests that there is a direct relation between porosity (and by inference, an inverse relation with bulk density) and the abundance of coarse granophyric or vapor-phase alteration. The samples that show the most abundant zones of coarse crystallization also have the highest measured porosities, regardless of the degree of welding shown by

flattening of shards and pumice. Although, in general, denser welding correlates with decreased porosity, secondary recrystallization resulting from slow cooling combined with late gas and fluid activity is important in producing small but significant porosity increases within densely welded tuffs. The magnitude of this increase is probably within the range of 1-3%.

Laboratory mechanical property results were obtained in compressive, constant strain rate tests over a range of saturation, confining pressure, and temperature conditions. The Young's modulus and strength data have, at most, a factor of 2 scatter at any given set of experimental conditions. In retrospect, because of the limited number of samples tested at any set of conditions, more tests need to be run at all sets of experimental conditions reported here in order to increase confidence in the resulting conclusions drawn from the data. Some meaningful conclusions, however, can be drawn.

Bulk modulus was found to be 10% higher in the saturated samples than in the dry samples run at 10 MPa effective pressure. This is the direct result of the water-filled voids having a much greater bulk stiffness than the dry, air-filled voids.

As is true for all silicic rocks, mean ultimate strength is directly related to effective confining pressure (0-10 MPa), with the calculated Coulomb failure criterion parameters ranging from 19 to 42 MPa in cohesion and from 31 to 57° in internal friction angle.

Young's modulus and strength are both inversely related to temperature. This effect, on average, is less than 20% over the temperature range 22-150°C.

The occurrence of higher-porosity textural features referred to above are responsible for the observed variability in mechanical properties. When relatively large regions of flattened lithophysae, pumice, and altered material occur within a laboratory test sample, both the Young's modulus and the strength of that sample is decreased. In addition, the test-induced fracture density is usually much greater within the highly porous pumice or altered zones than within the highly welded, low-porosity matrix. An open fracture can dominate the mechanical response of a sample. If the fracture is oriented at a low angle (less than ~50°) to the sample axis, the resulting ultimate strength is more indicative of the shear strength of the planar discontinuity than the intact rock strength. Conversely, healed fractures seem to have no effect on elastic or strength properties.

In addition, because the distribution of the high-porosity inhomogeneities (i.e., coarse granophyric crystallization) is nonuniform and the mechanical properties of the Topopah Spring Member are highly dependent on the occurrence of these features, the lateral distribution of mechanical property characteristics is probably also non-uniform.

Acknowledgements: The authors express their great appreciation for the work of M. E. Stavig and A. K. Jones, who measured, saturated/dried, and tested the samples. Thanks also to F. B. Nimick for his careful sample descriptions.

REFERENCES

- Bence, A. E., and Albee, A. L.**
Empirical Correction Factors for the Electron Probe Microanalysis of Silicates and Oxides, J. Geol., V. 76, 1968, p. 382-403.
- Brace, W. F.**
Brittle Fracture of Rocks, In: State of Stress in the Earth's Crust, W. R. Judd (ed.), New York: Elsevier, 1964, p. 111-174.
- Brown, W. L., and Parsons, I.**
Towards a more practical two-feldspar geothermometer, Contrib. Mineral. Petrol., V. 76, 1981, p. 369-377.
- Broxton, D. E., Byers, F. M., Jr., Warren, R. G., and Scott, R. B.**
Trends in phenocryst chemistry in the Timber Mountain-Oasis Valley volcanic field, S.W. Nevada: Evidence for episodic injection of primitive magma into an evolving magma system, (Abstract): Geol. Soc. Amer. Abstracts W. Programs, V. 17 (#6), 1986.
- Byers, F. M., Carr, W. J., Orkild, P. P., Quinlivan, W. D., and Sargent, K. A.**
Volcanic Suites and Related Cauldrons of Timber Mountain-Oasis Valley Caldera Complex, Southern Nevada, U. S. Geol. Survey Professional Paper 919, 1976.
- Carroll, P. I., Caporuscio, F. A., and Bish, D. L.**
Further description of the petrology of the Topopah Spring Member of the Paintbrush Tuff in drillholes UE25A#1 and USW G-1, and of the lithic-rich tuff in USW G-1, Yucca Mountain, Nevada, Los Alamos National Laboratory Report, LA-9000-MS, Los Alamos, NM, 1981.
- Chambers, W. F.**
SANDIA TASK-89: An Electron Microprobe Automation System, Sandia National Laboratories Report, SAND82-1081, Albuquerque, NM, 1983.
- Holcomb, D. J., and Jones, A. K.**
Data Acquisition for the Rock Mechanics Lab, Sandia National Laboratories Report, SAND83-0646, Albuquerque, NM, August 1983.
- Holcomb, D. J., and McNamee, M. J.**
Displacement Gage for the Rock Mechanics Laboratory, Sandia National Laboratories Report, SAND84-0651, Albuquerque, NM, December 1984.

Hugman, R. H. H., and Friedman, M.

Effects of Texture and Composition on Mechanical Behavior of Experimentally Deformed Carbonate Rocks, Amer. Assoc. Petr. Geol. Bull., V. 63 (#9), 1979, p. 1478-1489.

McNamee, M. J.

A Calibrator for Displacement Gages Used in the Rock Mechanics Laboratory, Sandia National Laboratories Report, SAND85-0548, Albuquerque, NM, May 1985.

Nimick, F. B., Price, R. H., VanBuskirk, R. G., and Goodell, J. R.

Uniaxial and Triaxial Compression Test Series on Topopah Spring Tuff from USW G-4, Yucca Mountain, Nevada, Sandia National Laboratories Report, SAND84-1101, Albuquerque, NM, December 1985.

Nimick, F. B., VanBuskirk, R. G., and MacFarland, A. J.

Uniaxial and Triaxial Compression Test Series on Topopah Spring Member from USW G-2, Yucca Mountain, Nevada, Sandia National Laboratories Report, SAND85-0703, Albuquerque, NM, in preparation.

Olsson, W. A.

Grain Size Dependence of Yield Stress in Marble, J. Geophys. Res., V. 79 (#32), 1974, p. 4859-4862.

Olsson, W. A., and Jones, A. K.

Rock Mechanics Properties of Volcanic Tuffs from the Nevada Test Site, Sandia National Laboratories Report, SAND80-1453, Albuquerque, NM, November 1980.

Price, R. H.

Analysis of Rock Mechanics Properties of Volcanic Tuff Units from Yucca Mountain, Nevada Test Site, Sandia National Laboratories Report, SAND82-1315, Albuquerque, NM, August 1983.

Price, R. H.

Effects of Sample Size on the Mechanical Behavior of Topopah Spring Tuff, Sandia National Laboratories Report, SAND85-0709, Albuquerque, NM, August 1986.

Price, R. H., and Bauer, S. J.

Analysis of the Elastic and Strength Properties of Yucca Mountain Tuff, Nevada, In: Research and Engineering Applications in Rock Masses, Vol. 1, Proc. 26th U.S. Symposium on Rock Mechanics, Eileen Ashworth (ed.), 1985, p. 89-96.

Price, R. H., and Jones, A. K.

Uniaxial and Triaxial Compression Test Series on Calico Hills Tuff, Sandia National Laboratories Report, SAND82-1314, Albuquerque, NM, October 1982.

- Price, R. H., Jones, A. K., and Nimick, K. G.
Uniaxial Compression Test Series on Bullfrog Tuff, Sandia National Laboratories Report, SAND82-0481, Albuquerque, NM, April 1982.
- Price, R. H., and Nimick, K. G.
Uniaxial Compression Test Series on Tram Tuff, Sandia National Laboratories Report, SAND82-1055, Albuquerque, NM, July 1982.
- Price, R. H., Nimick, F. B., Connolly, J. R., Keil, K., Schwartz, B. M., and Spence, S. J.
Preliminary Characterization of the Petrologic, Bulk; and Mechanical Properties of a Lithophysal Zone Within the Topopah Spring Member of the Paintbrush Tuff, Sandia National Laboratories Report, SAND84-0860, Albuquerque, NM, February 1985.
- Price, R. H., Nimick, K. G., and Zirzow, J. A.
Uniaxial and Triaxial Compression Test Series on Topopah Spring Tuff, Sandia National Laboratories Report, SAND82-1723, Albuquerque, NM, October 1982.
- Price, R. H., Spence, S. J., and Jones, A. K.
Uniaxial and Triaxial Compression Test Series on Topopah Spring Tuff From USW GU-3, Yucca Mountain, Southern Nevada, Sandia National Laboratories Report, SAND83-1646, Albuquerque, NM, February 1984.
- Scott, R.B., Spengler, R.W., Diehl, S., Lappin, A.R., and Chornack, M.P.
Geologic character of tuffs in the unsaturated zone at Yucca Mountain, southern Nevada, in Role of the unsaturated zone in radioactive and hazardous waste disposal, Ann Arbor Science Publishers, Ann Arbor, Michigan, 1983, p. 289-335.
- Selleck, C. B.
GRAPH III: A Digitizing and Graph Plotting Program, Sandia National Laboratories Report, SAND86-0525, Albuquerque, NM, March 1986.
- Sheridan, M. F., and Ragan, D. M.
Compaction of ash-flow tuffs, in Compaction of coarse-grained sediments II, Developments in Sedimentology V. 18B, Elsevier, 1976, p. 677-717.
- Spencer, K. J., and Lindsley, D. H.
A solution model for coexisting iron-titanium oxides, American Mineralogist, V. 66, 1981, p. 1189-1201.
- Stormer, J. C., Jr.
The effects of recalculation on estimates of temperature and oxygen fugacity from analyses of multicomponent iron-titanium oxides, American Mineralogist, V. 68, 1983, p. 586-594.

Stormer, J. C., Jr., and Whitney, J. A.

Two feldspar and iron-titanium oxide equilibria in silicic magmas and the depth of origin of large volume ash-flow tuffs, American Mineralogist, V. 70, 1985, p. 52-64.

Vaniman, D., Bish, D., Broxton, D., Byers, F., Heiken G., Carlos, B., Semarge, E., Caporuscio, F., and Gooley, R.

Variations in authigenic mineralogy and sorptive zeolite abundance at Yucca Mountain, Nevada, based on studies of drill cores USW GU-3 and G-3, Los Alamos National Laboratory Report, LA-9707-MS, Los Alamos, NM, 1984.

Warren, R. G., Byers, F. M., Jr., and Caporuscio, F. A.

Petrography and mineral chemistry of units of the Topopah Spring, Calico Hills and Crater Flat Tuffs, and older volcanic units, with emphasis on samples from drill hole USW G-1, Yucca Mountain, Nevada Test Site, Los Alamos National Laboratory Report, LA-10003-MS, Los Alamos, 1984.

Table 1.
Symbols, Definitions, Conventions and Units

SYMBOL	DEFINITION	UNITS
K	Elastic constant : Bulk modulus	GPa
E	Elastic constant : Young's modulus	GPa
ν	Elastic constant : Poisson's ratio	—
$\sigma_1, \sigma_2, \sigma_3$	Principal stresses, compressive stresses are positive	MPa
σ_{ax}	Stress parallel to the sample axis, ($\sigma_{ax} \approx \sigma_1$)	MPa
P_c	Confining pressure	MPa
P_p	Pore pressure	MPa
P_e	Effective confining pressure ($P_e = P_c - P_p$)	MPa
$\Delta\sigma$	Differential stress ($\Delta\sigma = \sigma_1 - \sigma_3 \approx \sigma_{ax} - P_c$)	MPa
$\Delta\sigma_u$	Ultimate differential stress	MPa
$\epsilon_1, \epsilon_2, \epsilon_3$	Principal strains, compressive strains are positive	—
ϵ_{ax}	Strain parallel to the sample axis ($\epsilon_{ax} \approx \epsilon_1$)	—
$\dot{\epsilon}_{ax}$	Axial strain rate	s ⁻¹
$(\epsilon_{ax})_u$	Axial strain at ultimate axial stress	—
ϵ_{lat}	Strain perpendicular to the sample axis ($\epsilon_{lat} \approx \epsilon_2 \approx \epsilon_3$)	—
ϵ_v	Volumetric strain ($\epsilon_v \approx \epsilon_1 + \epsilon_2 + \epsilon_3 \approx \epsilon_{ax} + 2\epsilon_{lat}$)	—
τ_0	Cohesion (inherent shear strength)	MPa
ϕ	Angle of internal friction	°
S	Saturation (Y : totally saturated ; N : oven dried)	—

Table 2.
Brief Descriptions of the Mechanical Test Samples

Sample ID	Description (from F. B. Nimick, personal communication)
10AE3W	One healed fracture cutting entire sample, 30° to sample axis, 3-4 other small healed fractures; small altered areas common.
10AE3Z	One healed fracture continuous around sample, system of small healed fractures at one end.
10AE4Y	Numerous small healed fractures; one lithic fragment, 7.5x6.0mm at 70° to sample axis.
10AE9X	One healed fracture intersects an end at 30° to sample axis, continuous from end to side of sample.
10AE10W	Two open lithophysal slits, one open lithophysis on sample end; one healed fracture continuous around sample, several partly open to healed radial fractures.
10AE12X	One open, flattened lithophysis, near middle, partly filled with calcite; minor pumice.
10AE12Z	One healed fracture, continuous around sample, ~30° to sample axis; one large pumice fragment; several lithics.
10AE14W	Minor fractures; several altered areas.
10AE14X	One lithic fragment, 12x12mm.
10AE15Y	One filled lithophysis at sample end; several fractures, one healed across end and down sides, two ~90° to sample axis.
10AE15Z	One mostly filled, flattened lithophysis; several small, healed fractures occur at both ends.
10AE20Z	Minor short, healed fractures.
10AE23X	One to two possible lithophysae, open; many small fractures, one intersects an end at 45° to sample axis; two altered areas intersecting ends.

Table 2. (continued)
Brief Descriptions of the Mechanical Test Samples

Sample ID	Description (from F. B. Nimick, personal communication)
10AE23Z	Minor fractures.
10AE24W	Three short interconnected lithophysae/fractures, locally healed, intersecting an end at 45-90°; two pumice with prominent void spaces; several small lithic fragments.
10AE24Y	Two closed lithophysae at 60° to sample axis, one intersects an end; several discontinuous fractures.
10AE25Y	One discontinuous fracture, open, 30° to sample axis; one altered area intersecting an end.
10AE25Z	Minor fractures; two minor altered areas intersecting ends.
10AE28X	One closed lithophysa, 40mm long, 80° to sample axis; two large altered areas, one of which intersects an end.
10AE29W	Many short, discontinuous fractures, all healed; altered areas of various sizes common.
10AE29Y	One possible fracture at 30° to sample axis.
10AE30Z	Two possible short lithophysae, mostly closed, one intersecting an end; several discontinuous fractures with two intersecting an end; two altered areas, one at an end.
10AE33X	One healed fracture at 80-90° to sample axis; several lithic fragments, one 12x12mm.
10AE34W	Several minor fractures, one circles sample at 90° to sample axis; one pumice ellipsoid, 18x37mm in middle of large altered area covering more than one-half of the sample volume in midsection of sample, portion of pumice missing from side of sample.
10AE34Z	One closed lithophysa, 25mm long at 85° to sample axis; minor healed fractures; one 50x75mm region of altered material and pumice with major axis ~90° to sample axis.

Table 2. (continued)
Brief Descriptions of the Mechanical Test Samples

Sample ID	Description (from F. B. Nimick, personal communication)
10AE35Y	One lithophysa, mostly closed, 37mm long, 85° to sample axis; minor healed fractures; one large altered area.
10AE38X	Minor healed fractures; common altered material and pumice, several ~10x30mm subperpendicular to sample axis.
10AE40W	Minor healed fractures; one altered region, 12x50mm that intersects an end.
10AE41Y	One partially open fracture intersecting an end at 20° to sample axis; large patch of altered material and pumice at other end; edges of sample ends chipped during machining.
10AE41Z	One altered area at one end.
10AE42X	One short, healed fracture across one end; minor pumice.
10AE43W	Several healed fractures at 80-90° to sample axis; one large pumice fragment; one large, altered area, 12x100mm.
10AE44X	One possible lithophysa, closed, 70-90° to sample axis; numerous short healed fractures, one intersects an end.
10AE45W	Possible lithophysae (grouped with fractures); four to five fractures, healed to partially open, 60-70° to sample axis; one large altered area covering one end and one-half of sample.
10AE46W	Several small, healed fractures; one entire end composed of altered material and pumice.
10AE47Y	One lithophysa ~15mm from end, mostly filled; minor healed fractures; numerous (~10%), small pumice.
10AE48Y	Numerous discontinuous, healed fractures; one lithic fragment, 12x18mm; two pumice fragments, one with hemispherical hole ~12 mm in diameter.
10AE50Y	Minor fractures; one altered area with some pumice at one end.
10AE52W	One altered area intersects an end.

Table 2. (concluded)
Brief Descriptions of the Mechanical Test Samples

Sample ID	Description (from F. B. Nimick, personal communication)
10AE52Z	One closed lithophysa, 50mm long, 80° to sample axis; one open fracture with circular outline on sample side; one very large altered area, ~50% of the sample volume.
10AE53Z	Minor fractures.
261A	Two healed fractures ~30° to sample axis and ~60° to each other, both intersect ends, first fracture has white filling, second is brown w/gray halo; possible fabric at 10-20° to sample axis.
261B	One large fragment (25×19mm); one healed fracture across one end 60° to sample axis, white filling w/gray halo, several other discontinuous healed fractures; one flattened lithophysa intersects opposite end from fracture; some inclusions with pink alteration halos, some pumice.
282A	One open lithophysa extends 65mm from an end at ~10° to sample axis, opening 0 to 8mm, partially filled with calcite(?), gray alteration halo, closed extension of lithophysa extends within 15mm of other end of sample; two healed fractures radiate from open lithophysa for 90mm at 0-30° to sample axis and at 20-45° to each other, a third open fracture extends from open lithophysa at 30-40° to sample axis.

Table 3a.
Summary of Mechanical Test Results from Dry Samples Tested at 22°C

ID	P_c (MPa)	$\dot{\epsilon}_{ax}$ (s ⁻¹)	K (GPa)	E (GPa)	ν	$\Delta\sigma_u$ (MPa)	$(\epsilon_{ax})_u$ (milli)
10AE24W	0	10 ⁻⁵	-	41.9	0.18	166.1	4.3
10AE34Z	0	10 ⁻⁵	-	33.7	0.24	135.2	5.3
10AE41Y	0	10 ⁻⁵	-	45.7	0.32	87.0	2.7
10AE46W	0	10 ⁻⁵	-	40.9	0.18	102.0	2.6
10AE28X	0	10 ⁻⁷	-	32.1	0.12	78.1	2.8
10AE30Z	0	10 ⁻⁷	-	37.0	0.18	157.1	4.6
10AE33X	0	10 ⁻⁷	-	42.2	0.20	185.5	4.8
10AE40W	0	10 ⁻⁷	-	40.6	0.17	182.8	4.7
10AE9X	5	10 ⁻⁵	14.8	37.9	0.21	220.2	7.3
10AE29Y	5	10 ⁻⁵	9.5	33.7	0.17	155.4	5.7
10AE52W	5	10 ⁻⁵	12.9	40.7	0.20	198.6	6.7
10AE25Z	10	10 ⁻⁵	17.6	40.8	0.19	304.5	8.1
10AE43W	10	10 ⁻⁵	13.9	33.1	0.24	182.8	9.7
10AE50Y	10	10 ⁻⁵	17.7	32.8	0.18	188.0	7.7

Table 3b.
Summary of Mechanical Test Results from Saturated Samples Tested at 22°C

ID	P_c (MPa)	$\dot{\epsilon}_{az}$ (s ⁻¹)	K (GPa)	E (GPa)	ν	$\Delta\sigma_u$ (MPa)	$(\epsilon_{az})_u$ (milli)
10AE23X	0	10 ⁻³	-	33.3	0.18	120.2	3.8
10AE24Y	0	10 ⁻³	-	36.8	0.19	169.0	4.7
10AE38X	0	10 ⁻³	-	33.1	0.23	95.5	3.0
10AE52Z	0	10 ⁻³	-	26.9	0.18	68.1	3.0
10AE12X	0	10 ⁻⁵	-	34.6	0.21	126.8	4.3
10AE15Z	0	10 ⁻⁵	-	37.4	0.20	158.4	4.4
10AE47Y	0	10 ⁻⁵	-	35.9	0.20	143.2	4.3
261A	0	10 ⁻⁵	-	45.7	0.20	200.5	4.8
261B	0	10 ⁻⁵	-	34.6	0.21	111.7	3.2
282B	0	10 ⁻⁵	-	34.6	0.20	104.3	3.4
10AE4Y	0	10 ⁻⁷	-	37.1	0.18	145.8	4.3
10AE25Y	0	10 ⁻⁷	-	42.1	0.21	94.3	2.3
10AE44X	0	10 ⁻⁷	-	44.5	0.23	149.0	3.8
10AE53Z	0	10 ⁻⁷	-	36.7	0.19	134.9	4.0
10AE14X	5	10 ⁻⁵	13.7	36.8	0.20	169.7	5.2
10AE23Z	5	10 ⁻⁵	12.8	37.1	0.21	198.7	6.7
10AE45W	5	10 ⁻⁵	10.6	35.5	0.21	169.0	6.7
10AE3Z	10	10 ⁻⁵	14.3	-	-	153.6	-
10AE10W	10	-	16.1	-	-	-	-
10AE12Z	10	10 ⁻⁵	16.9	32.5	0.19	186.5	7.6
10AE15Y	10	10 ⁻⁵	19.3	30.0	0.18	117.3	4.6
10AE20Z	10	10 ⁻⁵	22.1	32.9	0.18	193.3	8.7
10AE42X	10	10 ⁻⁵	19.8	35.2	0.19	151.7	6.0

Table 3c.
Summary of Mechanical Test Results from Saturated Samples Tested at 150°C

ID	P_c (MPa)	$\dot{\epsilon}_{az}$ (s ⁻¹)	K (GPa)	E (GPa)	ν	$\Delta\sigma_u$ (MPa)	$(\epsilon_{az})_u$ (milli)
10AE3W	0	10 ⁻⁵	-	30.6	-	135.8	5.7
10AE29W	0	10 ⁻⁵	-	32.6	-	129.7	5.3
10AE41Z	0	10 ⁻⁵	-	32.7	-	114.6	5.5
10AE48Y	0	10 ⁻⁵	-	28.0	-	89.4	4.9
10AE14W	5	10 ⁻⁵	-	33.9	-	155.2	6.2
10AE34W	5	10 ⁻⁵	-	16.0	-	47.9	6.4
10AE35Y	5	10 ⁻⁵	-	35.9	-	145.2	5.4

Table 4.
Statistical Summary of Mechanical Property Data

#	S	P_s (MPa)	$\dot{\epsilon}_{ax}$ (s ⁻¹)	T (°C)	K (GPa)	E (GPa)	ν	$\Delta\sigma_u$ (MPa)	$(\epsilon_{ax})_u$ (milli)
4	N	0	10 ⁻⁷	22	-	38.0±4.5	0.17±0.04	150.9±50.2	4.2±1.0
4	N	0	10 ⁻⁵	22	-	40.5±5.0	0.23±0.07	122.5±35.3	3.7±1.3
3	N	5	10 ⁻⁵	22	12.4±2.7	37.4±3.5	0.20±0.02	191.4±33.0	6.6±0.8
3	N	10	10 ⁻⁵	22	16.4±2.2	35.6±4.5	0.21±0.03	225.1±68.8	8.5±1.0
4	Y	0	10 ⁻⁷	22	-	40.1±3.8	0.20±0.02	131.0±25.2	3.6±0.9
6	Y	0	10 ⁻⁵	22	-	37.1±4.3	0.21±0.01	140.8±35.4	4.1±0.6
4	Y	0	10 ⁻³	22	-	32.5±4.1	0.20±0.02	113.2±42.8	3.6±0.8
3	Y	5	10 ⁻⁵	22	12.4±1.6	36.5±0.8	0.21±0.00	179.1±17.0	6.2±0.8
6	Y	10	10 ⁻⁵	22	18.1±2.8	32.6±2.1	0.18±0.01	160.5±30.6	6.7±1.8
4	Y	0	10 ⁻⁵	150	-	31.0±2.2	-	117.5±20.8	5.3±0.3
3	Y	5	10 ⁻⁵	150	-	28.6±11.0	-	116.1±59.3	6.0±0.5

Each value is the mean ± one standard deviation.

Table 5.
Coulomb Failure Criteria Values

S	P_c (MPa)	$\dot{\epsilon}_{ax}$ (s⁻¹)	T (°C)	τ_0 (MPa)	ϕ (°)
N	0,5,10	10 ⁻⁵	22	18.8	57.0
Y	0,5,10	10 ⁻⁵	22	41.7	30.6
Y	0,5	10 ⁻⁵	150	21.3*	50.0*

* Sample 34W data were excluded from the calculation of these values.

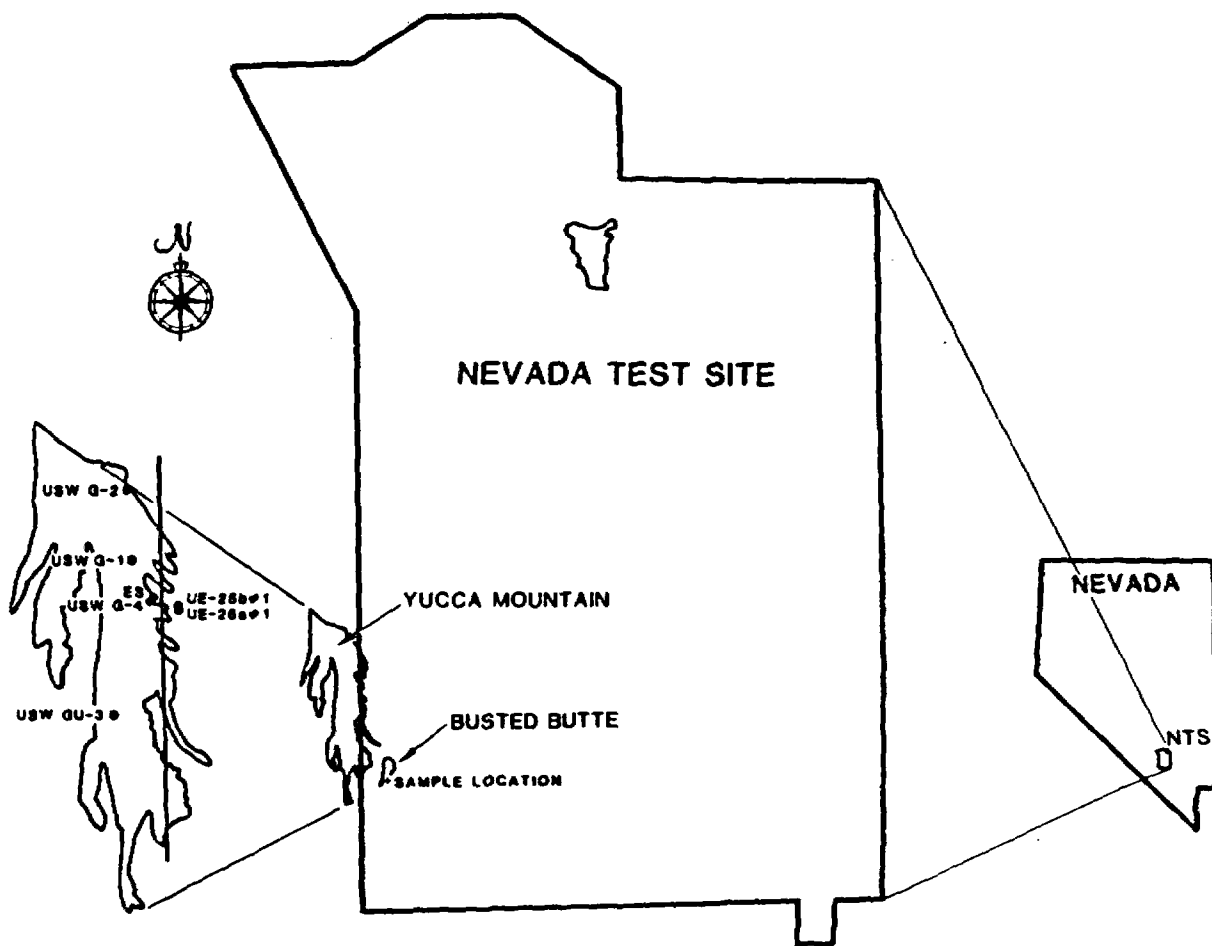


Figure 1. Map of Nevada Test Site, Yucca Mountain, and Busted Butte.

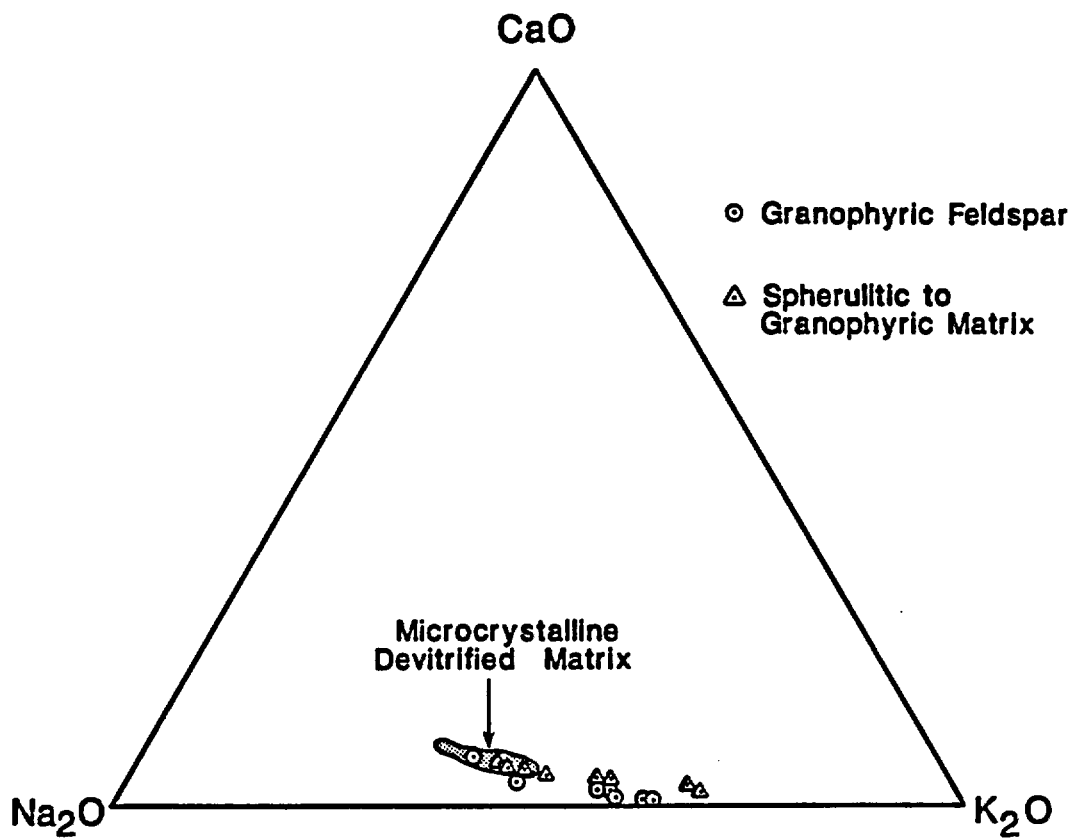


Figure 2. Molecular proportions, normalized to 100%, of CaO, Na₂O, and K₂O, for granophytic alkali feldspars and for different textural varieties of matrix from Rock #10 samples. Data represented in this diagram are given in Tables A-1 through A-3.

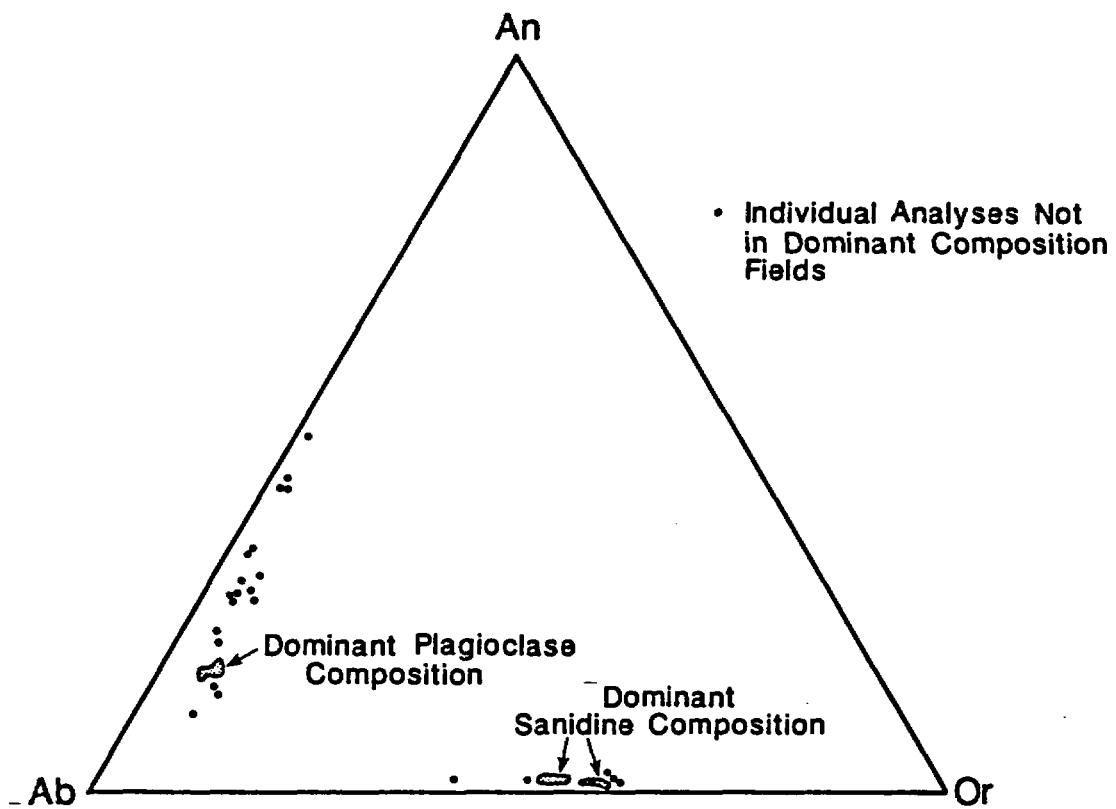


Figure 3. Composition of feldspar phenocrysts in terms of molecular endmembers albite (Ab - $\text{NaAlSi}_3\text{O}_8$), anorthite (An - $\text{CaAl}_2\text{Si}_2\text{O}_8$), and orthoclase (Or - KAlSi_3O_8) from Rock #10 samples. Data represented in this diagram are given in Tables A-4 and A-5.

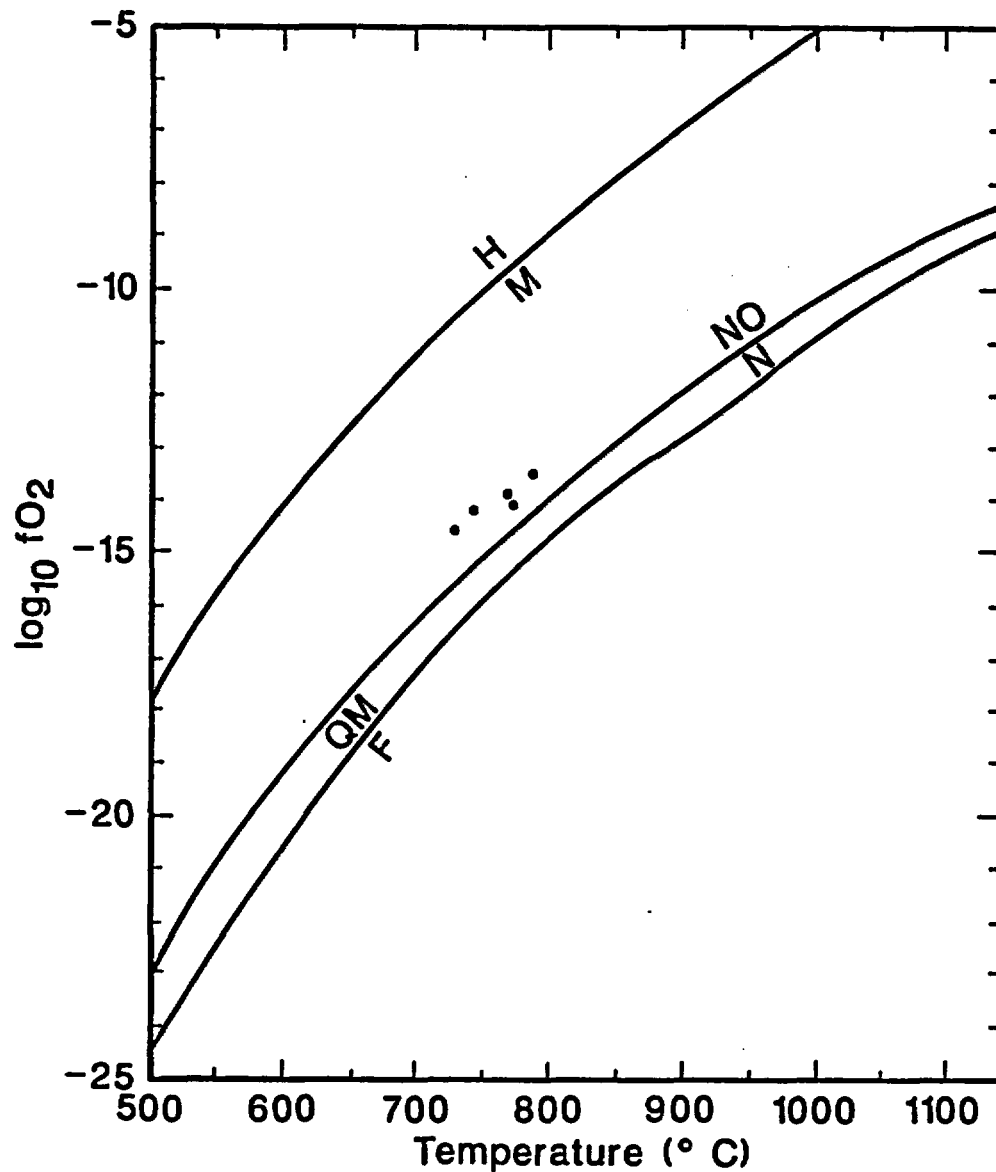


Figure 4. Temperature-oxygen fugacity (T- fO_2) diagram (after Spencer and Lindsley, 1981) showing Rock #10 Fe/Ti oxide results and position of various experimental buffers. Points shown are results from pairings of ilmenite and magnetite in individual samples with recalculated analytical totals greater than 97.5%. H/M: Hematite-Magnetite Buffer. NO/N: Nickel Oxide-Nickel Buffer. QM/F: Quartz-Magnetite-Fayalite Buffer. Data used to create this diagram are given in Table A-7.

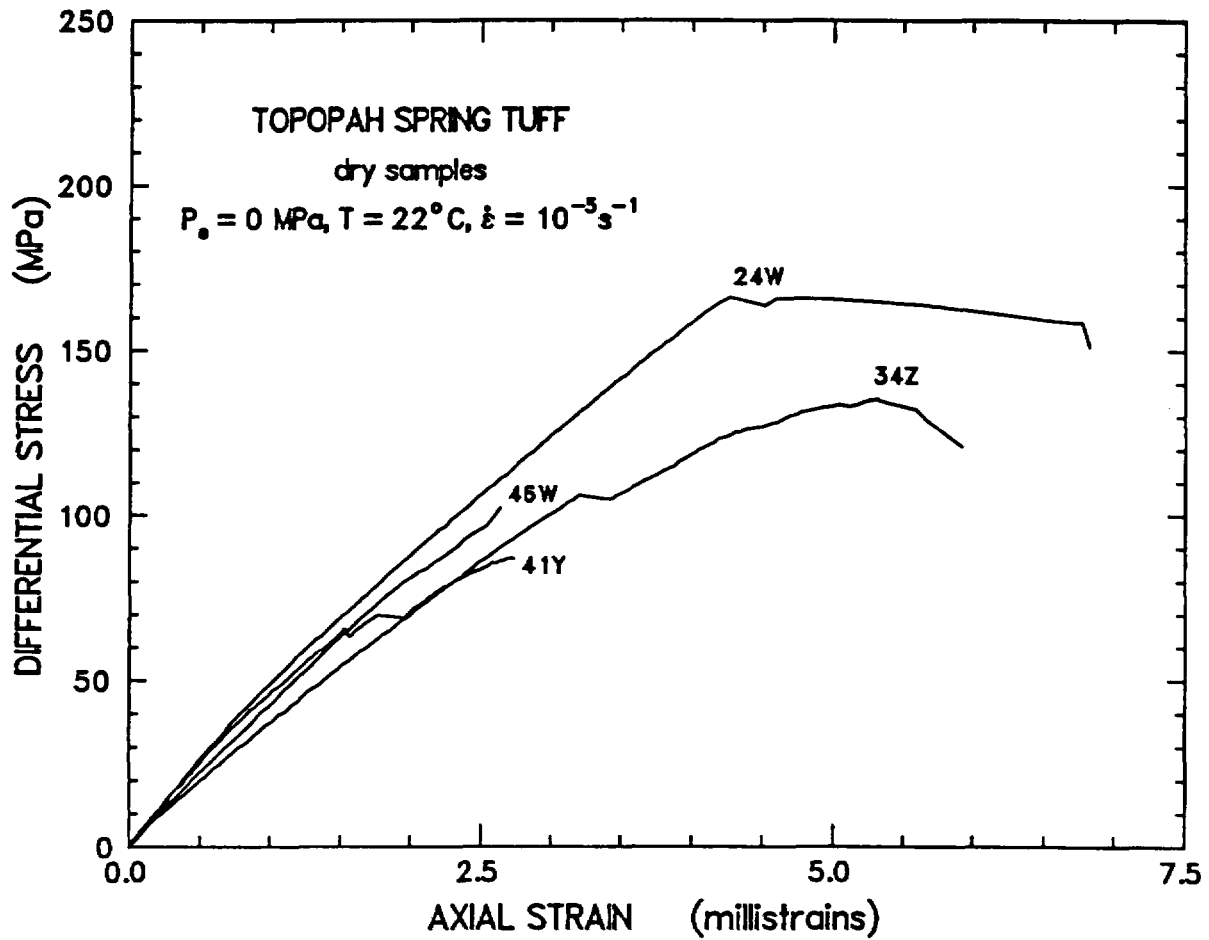


Figure 5a. Plots of differential stress versus axial strain for the four dry samples compressed at $P_0 = 0 \text{ MPa}$, $T = 22^\circ \text{C}$, and $\dot{\epsilon}_{ax} = 10^{-5} \text{ s}^{-1}$.

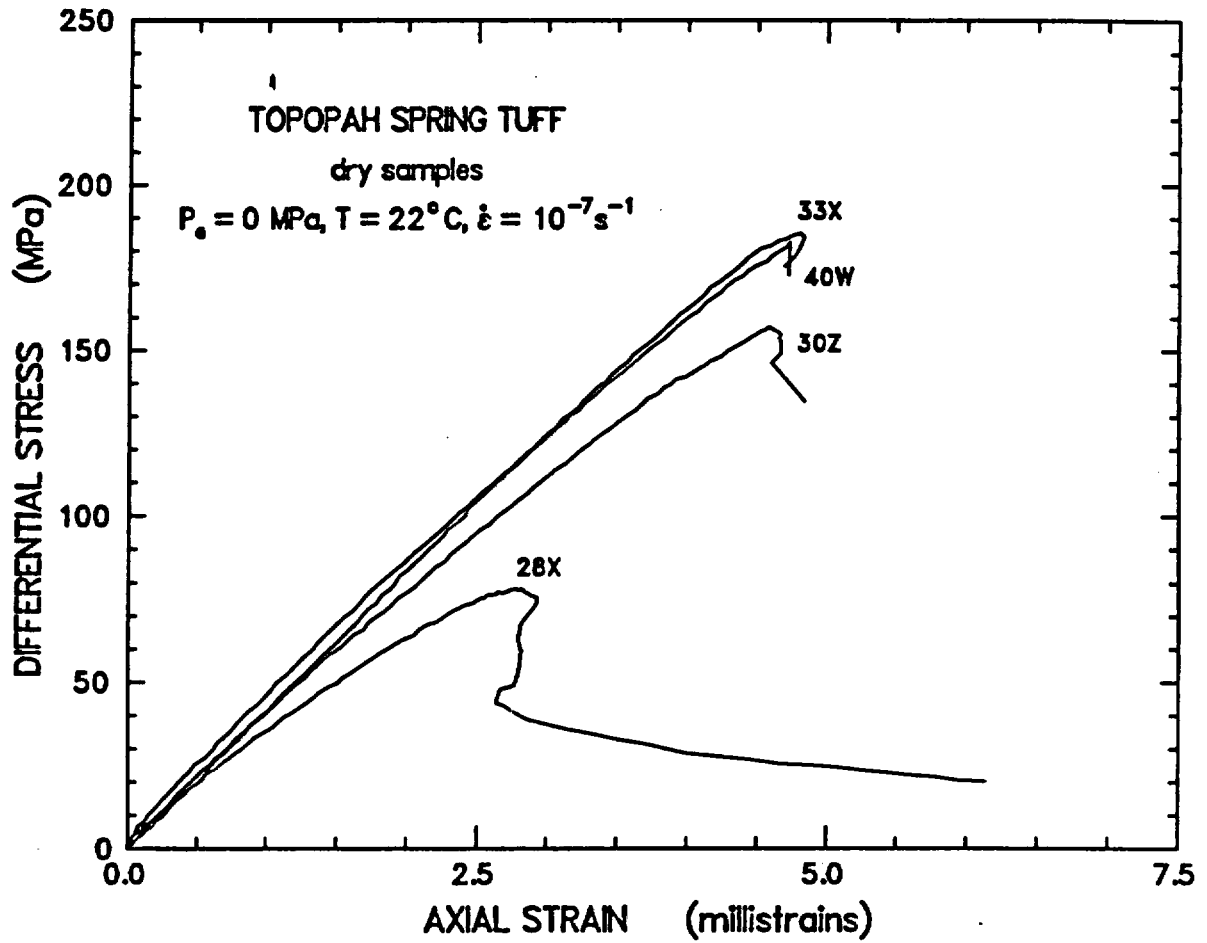


Figure 5b. Plots of differential stress versus axial strain for the four dry samples compressed at $P_e = 0 \text{ MPa}$, $T = 22^\circ \text{C}$, and $\dot{\epsilon}_{ax} = 10^{-7} \text{ s}^{-1}$.

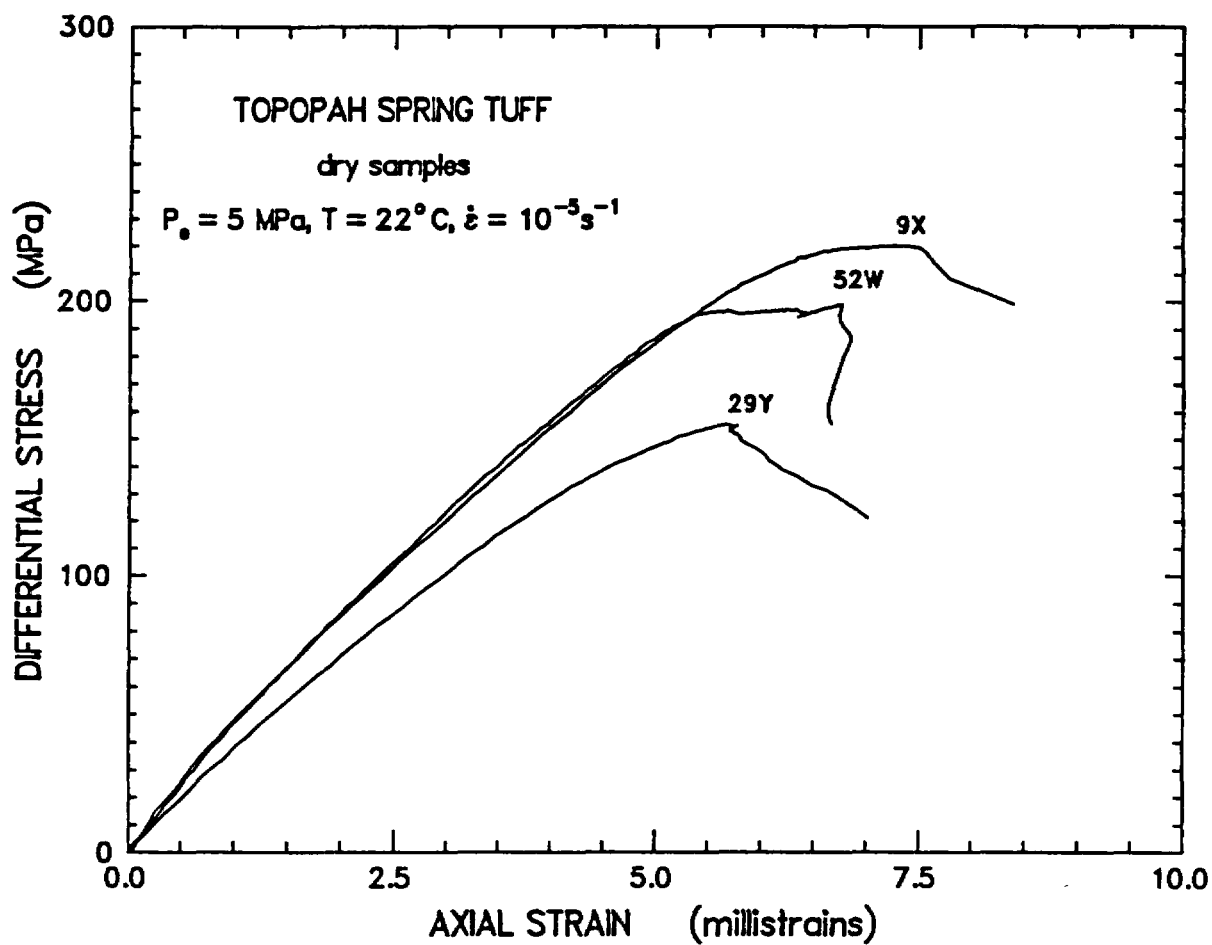


Figure 5c. Plots of differential stress versus axial strain for the three dry samples compressed at $P_e = 5 \text{ MPa}$, $T = 22^\circ \text{C}$, and $\dot{\epsilon}_{ax} = 10^{-5} \text{ s}^{-1}$.

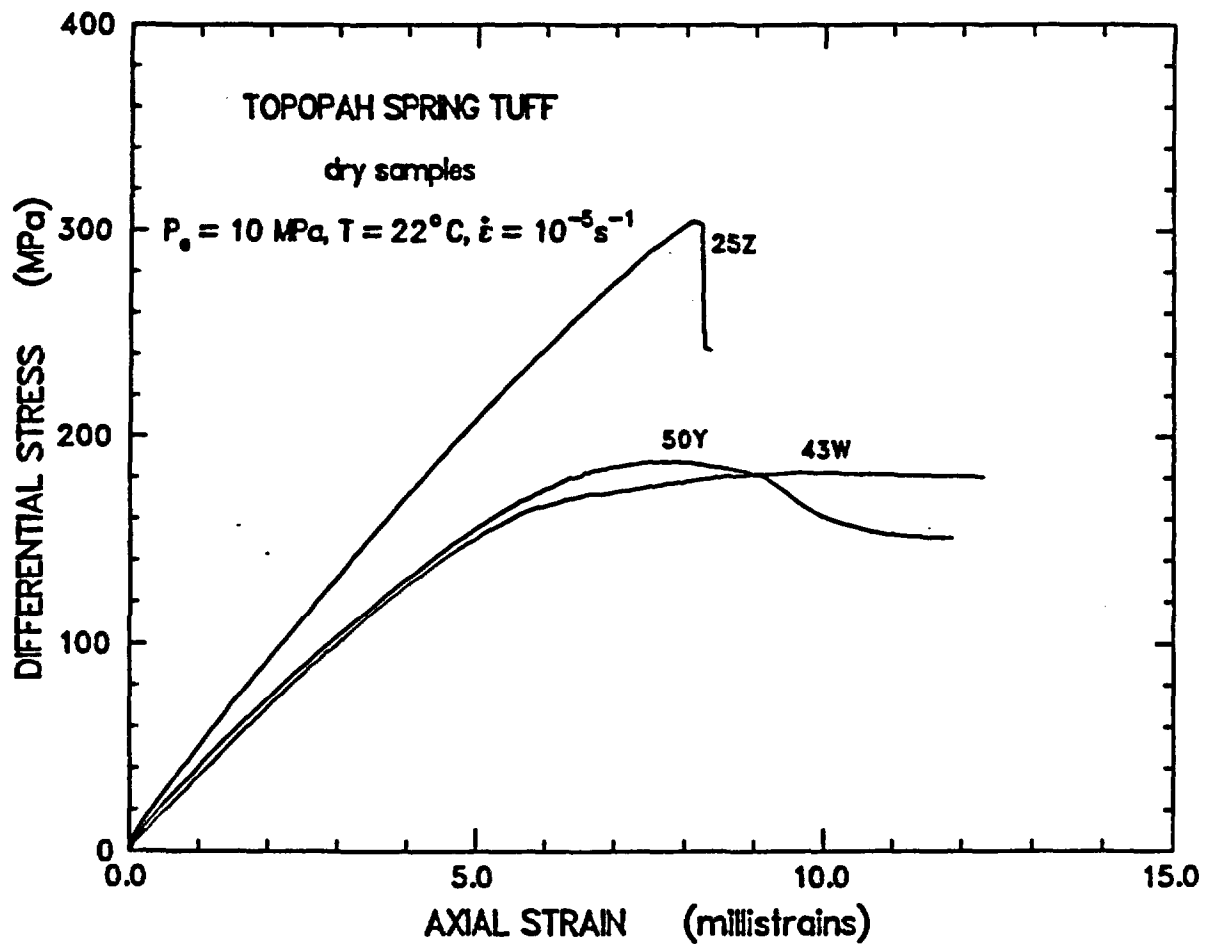


Figure 5d. Plots of differential stress versus axial strain for the three dry samples compressed at $P_e = 10 \text{ MPa}$, $T = 22^\circ\text{C}$, and $\dot{\epsilon}_{ax} = 10^{-5} \text{ s}^{-1}$.

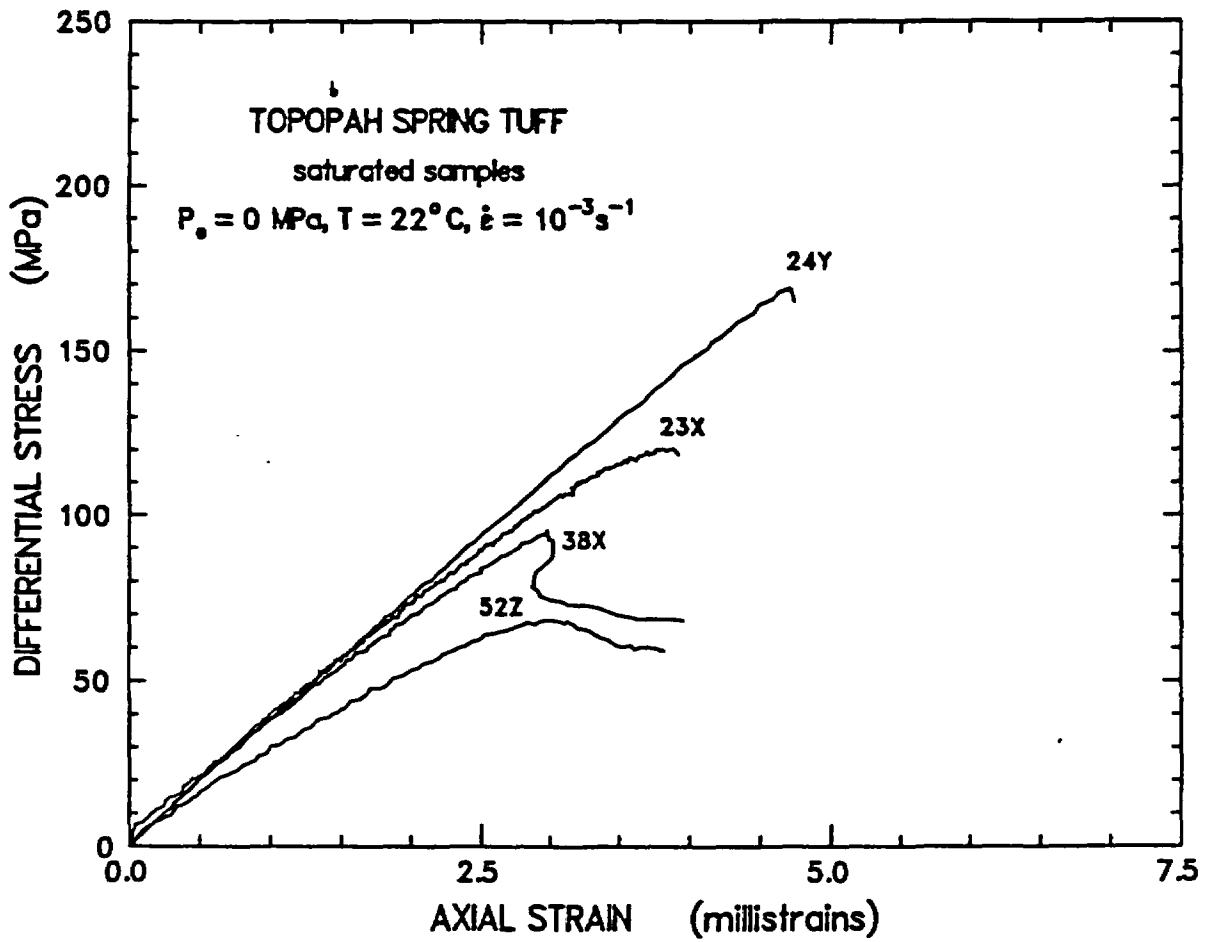


Figure 5e. Plots of differential stress versus axial strain for the four saturated samples compressed at $P_e = 0 \text{ MPa}$, $T = 22^\circ \text{C}$, and $\dot{\epsilon}_{ax} = 10^{-3} \text{ s}^{-1}$.

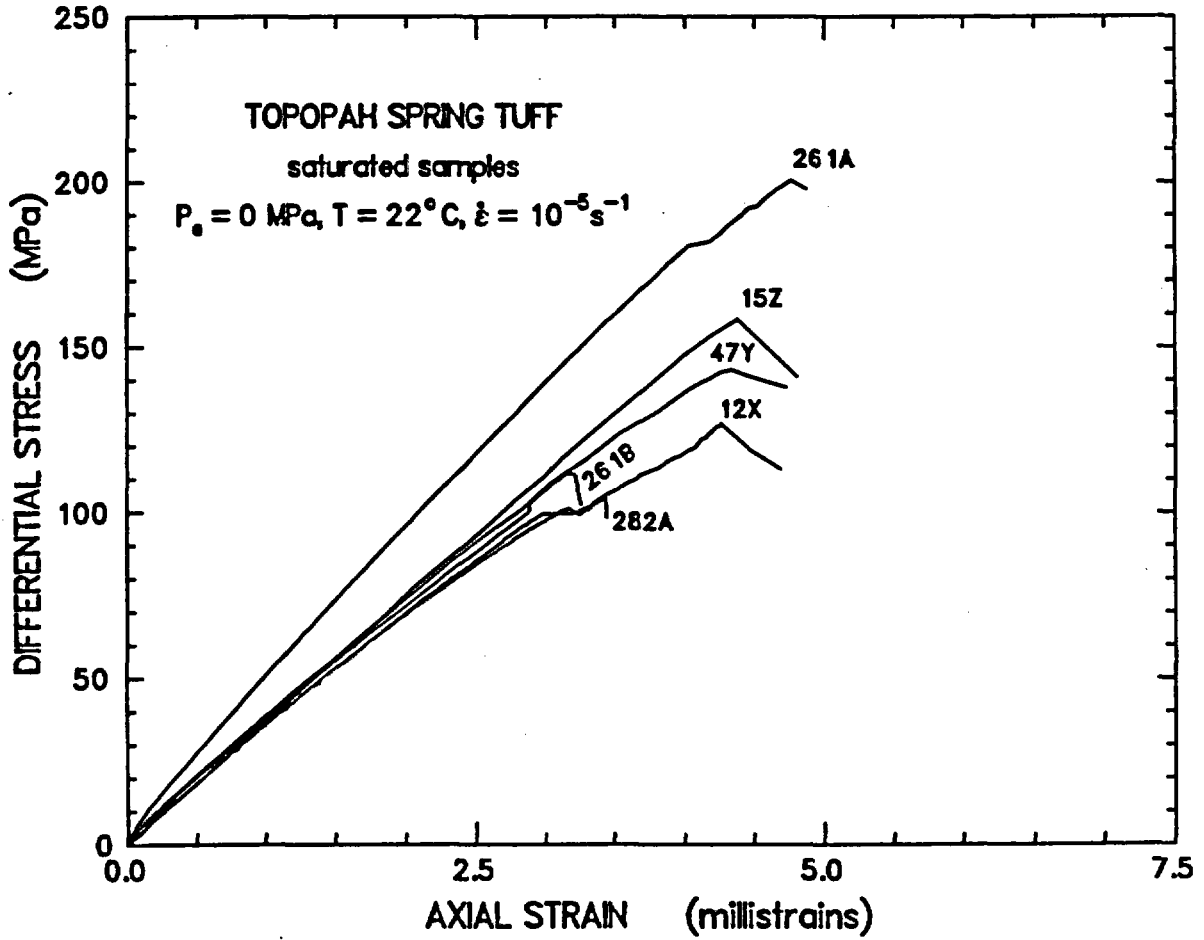


Figure 5f. Plots of differential stress versus axial strain for the six saturated samples compressed at $P_e = 0 \text{ MPa}$, $T = 22^\circ \text{C}$, and $\dot{\epsilon}_{ax} = 10^{-5} \text{ s}^{-1}$.

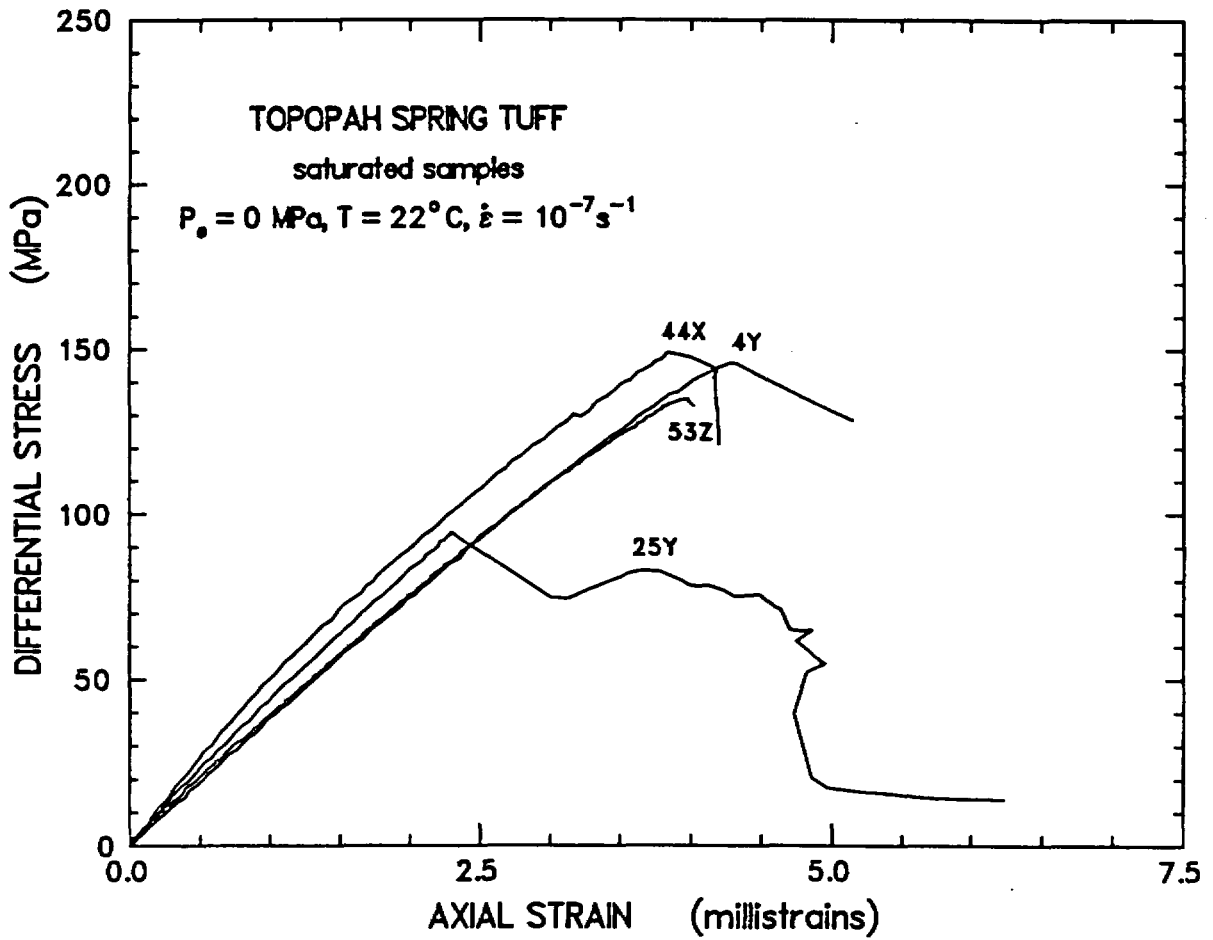


Figure 5g. Plots of differential stress versus axial strain for the four saturated samples compressed at $P_e = 0 \text{ MPa}$, $T = 22^\circ \text{C}$, and $\dot{\epsilon}_{ax} = 10^{-7} \text{ s}^{-1}$.

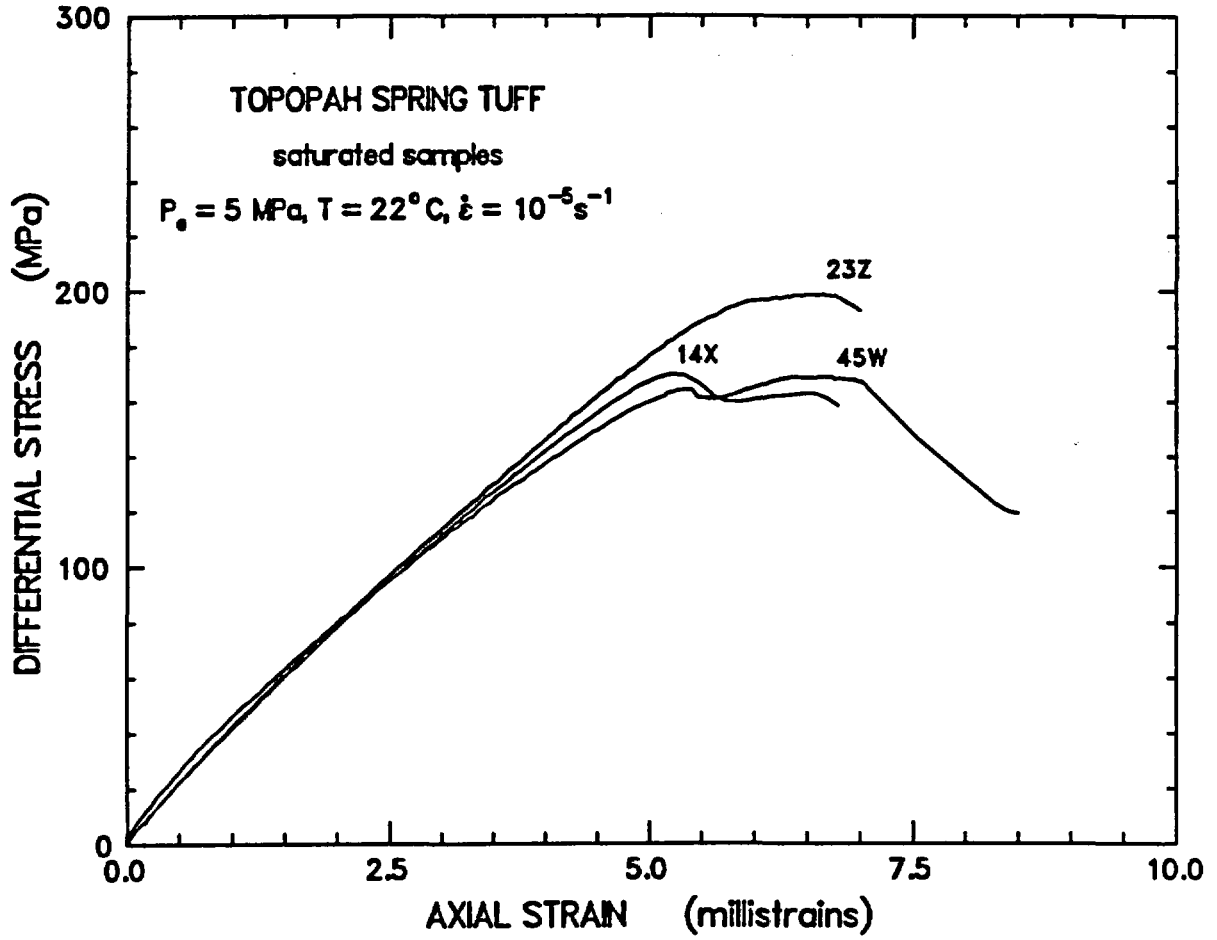


Figure 5h. Plots of differential stress versus axial strain for the three saturated samples compressed at $P_e = 5 \text{ MPa}$, $T = 22^\circ \text{C}$, and $\dot{\epsilon}_{ax} = 10^{-5} \text{ s}^{-1}$.

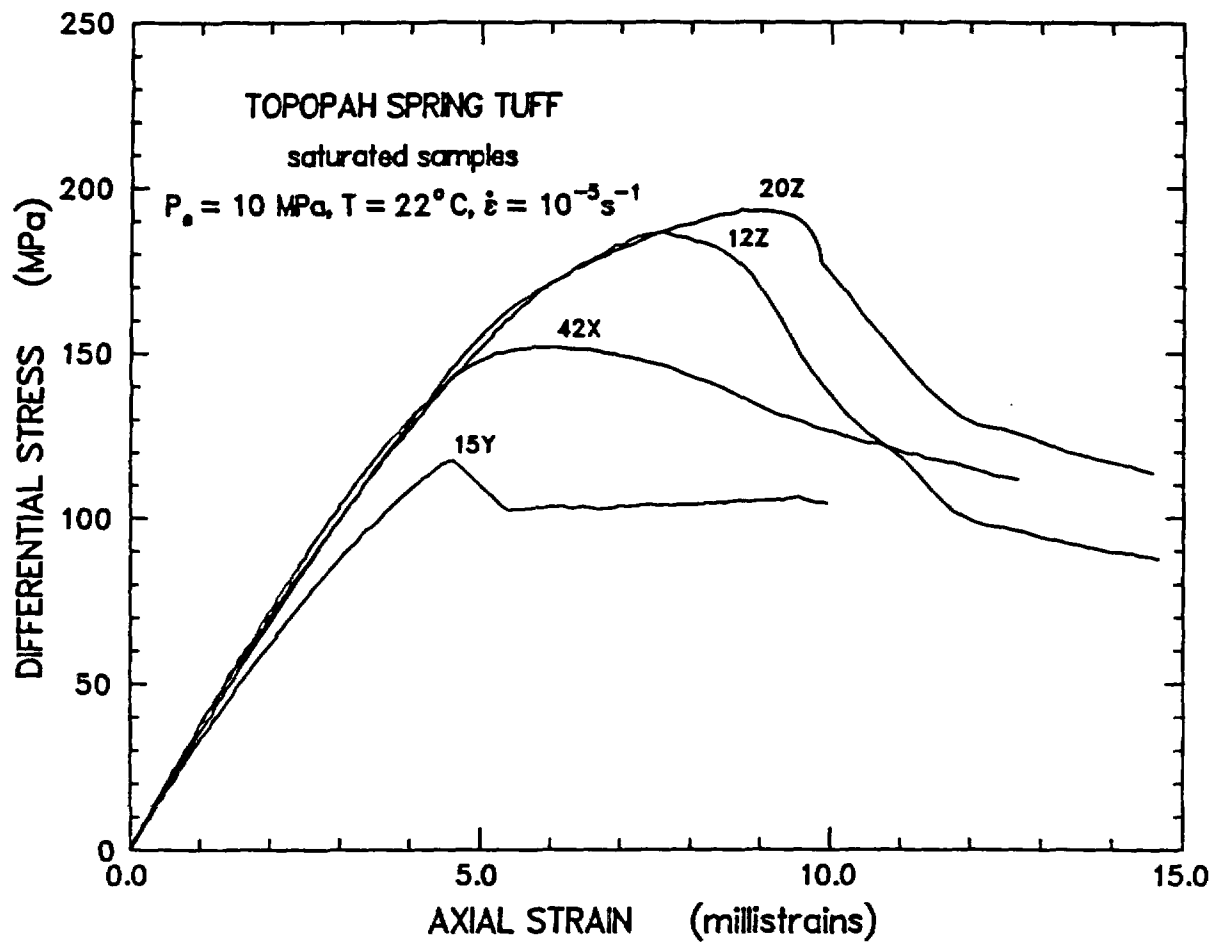


Figure 5i. Plots of differential stress versus axial strain for the four saturated samples compressed at $P_e = 10 \text{ MPa}$, $T = 22^\circ \text{C}$, and $\dot{\epsilon}_{ax} = 10^{-5} \text{ s}^{-1}$.

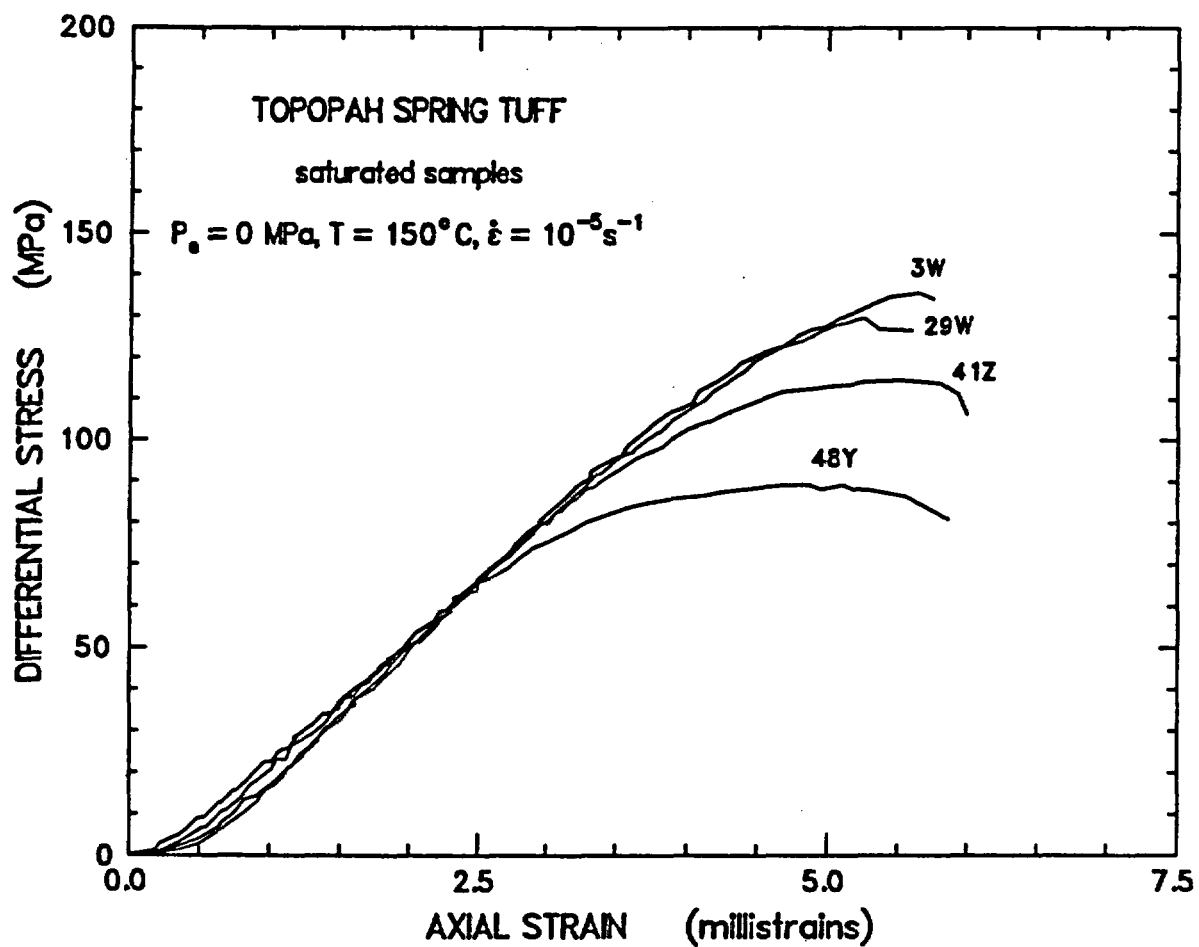


Figure 5j. Plots of differential stress versus axial strain for the four saturated samples compressed at $P_e = 0 \text{ MPa}$, $T = 150^\circ\text{C}$, and $\dot{\epsilon}_{ax} = 10^{-5} \text{ s}^{-1}$.

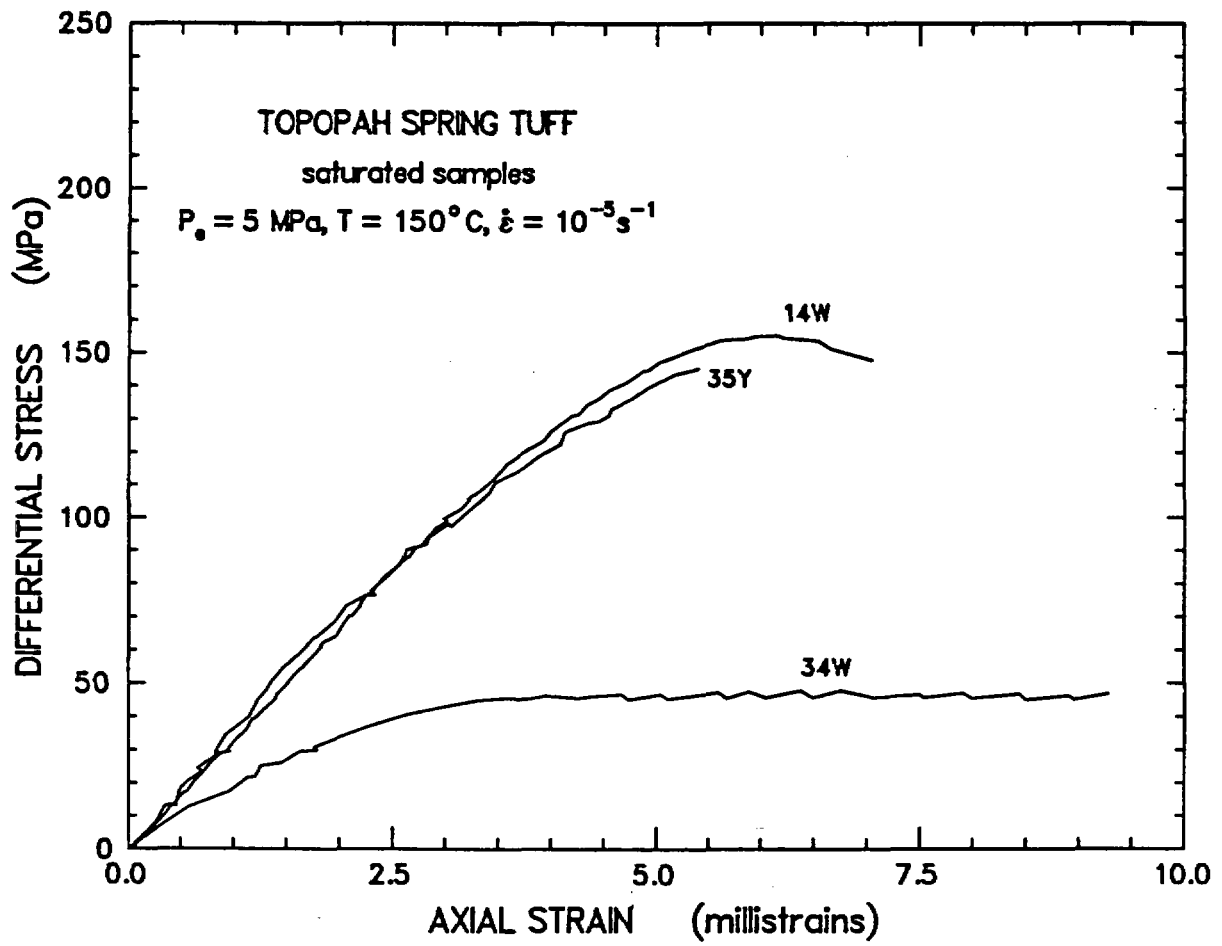


Figure 5k. Plots of differential stress versus axial strain for the three saturated samples compressed at $P_e = 5 \text{ MPa}$, $T = 150^\circ \text{C}$, and $\dot{\epsilon}_{ax} = 10^{-5} \text{ s}^{-1}$.

APPENDIX A

Petrologic Analysis Procedures and Data

Descriptive Petrology: All descriptive petrologic data are recorded on sample description forms. For each sample, a very brief hand sample description was prepared using a 10X hand lens; colors, textures, and any unusual fragments or alteration present were noted. This was followed by detailed microscopic descriptions of the welding fabric, extent, and texture of devitrification, and miscellaneous other features (including fractures, porosity characteristics, etc.). The forms also contain data on the source of the material and when the descriptions were made. The brief descriptions of the mechanical test samples by F. B. Nimick (Table 2) did not always use the same descriptive vocabulary as that used for these samples.

One rectangular polished thin section (25x45 mm) was made from each sample. The areas sectioned were chosen by visual inspection to be representative of the sample as a whole. Large transmitted light photographs (280x355 mm) were prepared for each section for use in marking features for microprobe and SEM study, and for visual estimation of proportions of phenocryst phases and fragment types. Description forms, photographs, and other notes are on file at the Institute of Meteoritics, University of New Mexico (UNM).

The sections were studied optically using a Carl Zeiss Research Microscope having both transmitted and reflected light capabilities. Fragment sizes were estimated using a micrometer eyepiece (the standard eyepiece for this microscope), and angular measurements of deformed shards were made using a rotating goniometer stage. Degree of welding was estimated qualitatively using the criteria of Carroll, Caporuscio, and Bish (1981) as outlined below:

Nonwelded:	No deformation of components.
Slightly Welded:	Minor shard deformation around phenocrysts.
Partly Welded:	Major shard deformation around phenocrysts; no flow deformation in groundmass.
Moderately Welded:	Major shard deformation around phenocrysts; deformation and flow in groundmass.
Densely Welded:	Pronounced shard deformation and alignment.
Vitrophyric:	Glassy, all vitric components deformed by welding and annealing (perlitic fractures may occur).

X-ray Diffraction: X-ray powder diffraction (XRD) was used for qualitative identification of finely crystalline minerals produced by devitrification. Samples analyzed were chosen from the hand samples to be representative of the rock as a whole, and included two samples of devitrified matrix (51Z and 27W) that were essentially free of vapor-phase alteration; a sample of porous, soft, vapor-phase altered material from 51Z; and a sample of surficial 'caliche' fill material (from 53W). The matrix samples were powdered in a SPEX brand tungsten-carbide ball mill prior to analysis, and the other material was powdered with a synthetic sapphire (Diamonite) mortar and pestle prior to analysis.

The powdered material was made into an aqueous suspension, spread evenly on a microscope slide, and allowed to dry. XRD data were obtained using an automated SCINTAG diffractometer utilizing nickel-filtered Cu K- α radiation. The X-ray tube was operated with an excitation potential of 40 kV and filament current of 30 mA, and data were gathered over an angular scanning range from 4 to 54° 2 θ . Data were stored on 133 mm floppy disks by the Data General Microcomputer used to operate the X-ray unit, and these data were graphically displayed in standard 2 θ /peak intensity plots. Minerals were identified by comparing peaks in the output to those in the Joint Committee on Powder Diffraction (JCPDS) powder diffraction file.

All X-ray data are on file at the Institute of Meteoritics, UNM.

Electron Microprobe Analyses: Electron microprobe analyses of devitrified matrix, fiamme, vapor-phase feldspars, and phenocrysts (feldspar, biotite, and Fe-Ti oxide) were made between August and December, 1986, using an automated five-spectrometer JEOL 733 Superprobe. Analyses were made on the same polished thin sections studied with the optical microscope using the large photo 'maps' to locate points analyzed. Analyses were carried out by wavelength dispersive techniques, using a 15 kV acceleration potential and various beam currents. Feldspars and matrix were analyzed with 0.01 μ A currents, and biotites and oxides were analyzed with 0.02 μ A currents. A broad (10-15 μ m diameter) electron beam was used for most analyses to minimize heating of samples during analysis. The microprobe is automated by the SANDIA TASK-83 electron microprobe automation package (Chambers, 1983), and differential matrix effects were corrected by the method of Bence and Albee (1968) as incorporated in the automation package.

Various feldspars, pyroxenes, and oxides were used as standards, depending on the material to be analyzed, and the instrument was calibrated prior to each analytical session.

Tables A-1 through A-7 summarize the electron microprobe data. Amounts shown as below detection limit (* in tables) are amounts for a single analysis. Since most analyses are an average of several points, these were included in the totals and norm

calculations. Effects on these calculations are very minor. Complete data, including polished thin sections, large photo 'maps', probe data output, and probe data summary sheets are on file at the Institute of Meteoritics, UNM.

Scanning Electron Microscopy: A Hitachi S-450 Scanning Electron Microscope (SEM) was used to study pore distribution characteristics and produce photographic images of the polished surfaces of the thin sections. The density contrast between the minerals and the epoxy used to fill pores results in a strong contrast between the rock and the pores (which appear darker) in both the secondary electron (SE) and the back-scattered electron (BSE) images. Because some pores can be the result of plucking of grains during the thin section preparation process, the technique is not rigorously quantitative, but can show qualitative differences in pore distribution in various matrix types (i.e., vapor-phase altered versus devitrified).

Table A-1: Defocused Beam Electron Microprobe Analyses (in wt%) of Devitrified Matrix

<u>Analysis Number</u>	<u>1</u>	<u>2</u>	<u>3</u>	<u>4</u>	<u>5</u>	<u>6</u>	<u>7</u>	<u>8</u>	<u>9</u>
Sample	7Y	7Y	7Y	27W	27W	27X	31Y	31Z	33Z
# points avgd.	22	18	4	24	10	24	22	25	19
<u>Oxide Wt %</u>									
SiO ₂	78.0	77.9	78.3	79.7	77.5	77.8	77.4	79.4	75.3
TiO ₂	0.03*	0.04	0.0*	0.05	0.11	0.04	0.01*	0.08	0.08
Al ₂ O ₃	10.7	10.6	11.2	9.29	10.4	10.7	11.4	9.84	11.5
FeO	0.66	0.74	0.24	0.72	0.54	0.46	0.45	0.60	0.81
MnO	0.02*	0.02*	0.01*	0.04*	0.05	0.02*	0.01*	0.01*	0.02*
MgO	0.04	0.05	0.01*	0.03	0.03	0.04	0.04	0.03	0.04
BaO	0.0*	0.0*	0.0*	0.01*	0.03*	0.01*	0.01*	0.01*	0.04*
CaO	0.50	0.51	0.46	0.34	0.30	0.34	0.37	0.43	0.33
Na ₂ O	3.92	3.85	4.18	2.94	3.22	3.46	3.48	3.47	3.43
K ₂ O	3.61	3.53	3.93	3.80	4.58	4.39	4.89	3.44	5.10
<hr/>	<hr/>	<hr/>	<hr/>	<hr/>	<hr/>	<hr/>	<hr/>	<hr/>	<hr/>
Total	97.5	97.2	98.3	96.9	96.8	97.3	98.1	97.3	96.7
CaO**	8.1	8.4	7.0	6.5	5.1	5.5	5.7	7.7	5.1
Na ₂ O**	57.2	57.1	57.5	50.5	49.0	51.3	50.0	55.9	48.0
K ₂ O**	34.7	34.5	35.5	43.0	45.9	43.2	44.3	36.4	46.9
Na/K (molecular)	1.65	1.66	1.62	1.18	1.06	1.20	1.08	1.53	1.02
<u>Molecular Norms:</u>									
Quartz	38.49	39.07	36.24	45.63	39.27	38.54	35.71	43.46	33.51
Orthoclase	22.14	21.73	23.80	23.77	28.43	27.04	29.80	21.27	31.53
Albite	36.55	36.02	38.48	27.95	30.38	32.39	32.24	32.61	32.23
Anorthite	0.97	1.27	0.20	0.98	0.42	0.73	1.08	1.17	0.96
Diopside	1.28	1.10	0.85	0.64	0.92	0.82	0.65	0.85	0.60
Hypersthene	0.53	0.77		0.97	0.43	0.42	0.51	0.53	1.05
Ilmenite	0.04	0.06		0.07	0.16	0.06	0.01	0.12	0.12
Wollastonite			0.43						
<hr/>	<hr/>	<hr/>	<hr/>	<hr/>	<hr/>	<hr/>	<hr/>	<hr/>	<hr/>
Notes:	1	1R	1G	1	2	1	1	1	1

Explanation of Notes: * Amounts shown are as reported, but are below detection limit for an individual analysis.

** Molecular proportions, normalized to 100%.

1: Devitrified Shard Matrix (R=red, G=gray)

2: Fine Spherulitic Matrix

3: Fine Mosaic and Shard Matrix

4: Granophyric Matrix

Table A-1: Defocused Beam Electron Microprobe Analyses (in wt%) of Devitrified Matrix (Concluded)

<u>Analysis Number</u>	<u>10</u>	<u>11</u>	<u>12</u>	<u>13</u>	<u>14</u>	<u>15</u>	<u>16</u>
Sample	35Z	39X	51X	51Z	51Z	53W	53W
# points avgd.	23	25	18	20	16	25	21
<u>Oxide Wt %</u>							
SiO ₂	76.3	77.0	76.5	80.2	69.9	76.1	79.4
TiO ₂	0.08	0.06	0.04	0.07	0.04	0.10	0.04
Al ₂ O ₃	11.1	10.8	11.2	8.67	11.0	11.2	9.77
FeO	0.87	0.75	0.36	0.95	0.50	0.95	0.48
MnO	0.05	0.03*	0.02*	0.05	0.04	0.03*	0.01*
MgO	0.09	0.05	0.04	0.03	0.11	0.05	0.04
BaO	0.01*	0.02*	0.01*	0.05*	0.05*	0.0*	0.01*
CaO	0.41	0.42	0.29	0.33	0.38	0.48	0.40
Na ₂ O	3.52	3.50	3.41	2.94	3.28	3.83	3.38
K ₂ O	4.50	4.31	4.92	3.40	4.59	4.14	3.73
<u>Total</u>	<u>96.9</u>	<u>96.9</u>	<u>96.8</u>	<u>96.7</u>	<u>89.9</u>	<u>96.9</u>	<u>97.3</u>
CaO**	6.5	4.7	4.6	6.6	6.2	7.5	7.0
Na ₂ O**	50.8	50.2	48.9	53.0	48.8	54.1	53.9
K ₂ O**	42.7	45.1	46.5	40.4	45.0	38.4	39.1
Na/K (molecular)	1.19	1.23	1.05	1.31	1.09	1.41	1.38
<u>Molecular Norms:</u>							
Quartz	35.85	37.57	35.83	47.97	33.21	35.16	43.12
Orthoclase	27.78	26.63	30.38	21.32	30.48	25.52	23.07
Albite	33.02	32.87	32.01	28.02	33.10	35.88	31.77
Anorthite	1.25	1.08	0.76	0.44	1.80	1.19	0.49
Diopside	0.70	0.88	0.60	1.03	0.26	1.03	1.27
Hypersthene	1.28	0.88	0.37	1.11	1.09	1.07	0.22
Ilmenite	0.12	0.09	0.06	0.10	0.06	0.15	0.06
<u>Notes:</u>	2	2	1	3	4	1R	1G

Explanation of Notes: * Amounts shown are as reported, but are below detection limit for an individual analysis.

** Molecular proportions, normalized to 100%.

1: Devitrified Shard Matrix (R=red, G=gray)

2: Fine Spherulitic Matrix

3: Fine Mosaic and Shard Matrix

4: Granophyric Matrix

Table A-2: Defocused Beam Electron Microprobe Analyses (in wt%)
of Fiamme Matrix

Analysis Number	1	2	3	4	5	6
Sample	27W	31Y	31Y	35Z	51X	53W
# points avgd.	10	9	6	14	21	15
<u>Oxide Wt %</u>						
SiO ₂	79.9	59.2	82.5	66.8	68.4	61.4
TiO ₂	0.06	0.05	0.05	0.04	0.03	0.03
Al ₂ O ₃	9.27	16.0	8.86	11.2	11.7	16.9
FeO	0.21	0.53	0.43	0.54	0.30	0.56
MnO	0.02*	0.01*	0.03*	0.01*	0.02*	0.02*
MgO	0.02	0.04	0.04	0.08	0.03	0.05
BaO	0.04*	0.03*	0.01*	0.02*	0.02*	0.03*
CaO	0.25	0.22	0.17	0.34	0.22	0.19
Na ₂ O	2.93	3.10	2.24	3.63	2.81	3.17
K ₂ O	4.27	9.81	4.81	4.73	5.57	10.6
<hr/>	<hr/>	<hr/>	<hr/>	<hr/>	<hr/>	<hr/>
Total	98.0	89.0	99.1	87.4	89.1	93.0
CaO**	4.4	2.5	3.4	5.3	3.6	2.0
Na ₂ O**	47.1	31.6	40.0	51.0	41.8	30.6
K ₂ O**	48.5	65.9	56.6	43.7	54.6	67.4
Na/K (molecular)	0.972	0.480	0.708	1.17	0.767	0.455
<u>Molecular Norms:</u>						
Quartz	45.53	2.81	48.57	28.28	31.44	1.49
Orthoclase	26.58	64.27	29.47	32.09	37.28	66.44
Albite	26.73	30.87	20.68	37.42	28.59	30.20
Anorthite		0.85		0.34	1.24	0.61
Diopside	0.69	0.29	0.70	1.28		0.31
Hypersthene		0.83	0.43	0.53	0.61	0.90
Ilmenite	0.09	0.08	0.07	0.06	0.05	0.04
Na-metasilicate	0.20		0.07			
Wollastonite	0.18					
Corundum					0.80	
<hr/>	<hr/>	<hr/>	<hr/>	<hr/>	<hr/>	<hr/>
Notes:	1S	2S	1G	1S	1S	2S

Explanation of Notes: * Amounts shown are as reported, but are below detection limit for an individual analysis.

** Molecular proportions, normalized to 100%

1: Rhyolitic (S=Spherulitic G=Granophyric)

2: Quartz Latitic (S=Spherulitic G=Granophyric)

**Table A-3: Electron Microprobe Analyses of Feldspars Crystallized
During Devitrification**

<u>Analysis Number</u>	<u>1</u>	<u>2</u>	<u>3</u>	<u>4</u>	<u>5</u>	<u>6</u>	<u>7</u>	<u>8</u>
Sample	7Y	7Y	31Y	31Y	31Y	35Z	53W	53W
# points avgd.	8	2	7	4	2	14	9	3
<u>Oxide Wt %</u>								
SiO ₂	66.4	65.8	66.2	66.4	65.9	65.8	65.9	66.4
Al ₂ O ₃	18.0	18.1	18.5	18.3	19.1	18.5	18.2	18.6
FeO	0.09	0.09	0.10	0.05	0.11	0.11	0.02*	0.02*
BaO	0.01*	0.0*	0.03*	0.02*	0.0*	0.01*	0.0*	0.0*
CaO	0.09	0.09	0.24	0.14	0.76	0.27	0.19	0.33
Na ₂ O	4.08	4.19	4.64	4.57	6.50	4.81	4.53	5.85
K ₂ O	10.56	10.43	9.85	9.78	7.06	9.66	9.92	7.99
<u>Total</u>	<u>99.2</u>	<u>98.7</u>	<u>99.6</u>	<u>99.3</u>	<u>99.4</u>	<u>99.2</u>	<u>98.8</u>	<u>99.2</u>
An**	0.5	0.5	1.2	0.7	3.6	1.3	0.9	1.6
Ab**	36.8	37.7	41.2	41.2	56.2	42.5	40.6	51.8
Or**	62.7	61.8	57.6	58.1	40.2	56.2	58.5	46.6
Na/K (molecular)	0.587	0.611	0.716	0.710	1.40	0.757	0.694	1.11
<u>Notes:</u>	1	2	1	2	1	3	3	3

Explanation of Notes: * Amounts shown are as reported, but are below detection limit for an individual analysis.

** Feldspar endmembers, molecular proportions, normalized to 100%.

1: Sanidine in fiamme

2: Sanidine in matrix

3: Sanidine in fiamme and matrix

Table A-4: Representative Electron Microprobe Analyses (in wt%) of Plagioclase Phenocrysts

Analysis Number	1	2	3	4	5	6	7	8	9	10	11	12	13
Sample	7Y	7Y	27X	31Y	31Y	31Y	31Z	33Z	35Z	39X	51X	51X	51Z
# points avgd.	8	1	5	6	2	2	5	14	8	11	6	2	7
Oxide Wt %													
SiO ₂	63.6	55.6	63.6	64.3	59.7	57.3	62.7	63.4	63.8	63.4	63.4	59.5	63.7
Al ₂ O ₃	22.0	26.1	22.0	21.9	25.2	26.6	21.9	22.3	21.8	22.3	22.2	24.7	21.9
FeO	0.13	0.26	0.18	0.08	0.01*	0.07	0.18	0.15	0.21	0.16	0.04*	0.16	0.15
BaO	0.02*	0.08	0.0*	0.07	0.12	0.08	0.01*	0.06*	0.01*	0.0*	0.0*	0.13	0.0*
CaO	3.64	8.79	3.63	3.45	6.81	8.55	3.67	3.61	3.07	3.60	3.61	6.35	3.52
Na ₂ O	9.00	6.38	8.88	8.93	7.45	6.51	9.00	8.85	9.17	8.94	8.91	7.60	9.04
K ₂ O	1.18	0.36	1.17	1.33	0.53	0.36	1.16	1.23	1.39	1.18	1.23	0.61	1.22
Total	99.6	97.6	99.5	100.1	99.8	99.5	98.6	99.6	99.4	99.6	99.4	99.1	99.5
An**	17.1	42.3	17.2	16.3	32.6	41.2	17.2	17.1	14.5	17.0	17.0	26.5	16.5
Ab**	76.3	55.6	76.1	76.2	64.4	56.7	76.3	75.9	77.7	76.4	76.1	67.4	76.7
Or**	6.6	2.1	6.6	7.5	3.0	2.1	6.5	7.0	7.8	6.6	6.9	6.1	6.8
Na/K (molecular)	11.6	26.9	11.5	10.2	21.4	27.5	11.8	10.9	9.97	11.5	11.0	11.0	11.3
Notes:	1	2	1	1	2	2	1	1	1	1	1	2	1

Explanation of Notes: * Amounts shown are as reported, but are below detection limit for an individual analysis.

** Feldspar endmembers, molecular proportions, normalized to 100%

1. Plagioclase of typical composition

2. Calcic Plagioclase

Table A-5: Representative Electron Microprobe Analyses (in wt%) of Sanidine Phenocrysts

<u>Analysis Number</u>	<u>1</u>	<u>2</u>	<u>3</u>	<u>4</u>	<u>5</u>	<u>6</u>	<u>7</u>	<u>8</u>	<u>9</u>	<u>10</u>	<u>11</u>	<u>12</u>	<u>13</u>
Sample	7Y	7Y	27W	27X	31Y	31Y	31Z	31Z	33Z	35Z	51X	51Z	53Z
# points avgd.	1	1	4	3	1	1	6	6	3	2	4	6	3
<u>Oxide Wt %</u>													
SiO ₂	65.4	65.0	65.0	65.6	66.2	66.4	65.4	65.0	65.5	65.3	65.1	65.7	65.6
Al ₂ O ₃	18.7	18.8	18.6	18.7	18.8	18.8	18.6	18.6	19.0	18.7	18.9	18.6	18.7
FeO	0.09	0.10	0.10	0.12	0.13	0.03*	0.15	0.18	0.15	0.17	0.02*	0.18	0.16
BaO	0.16	0.13	0.03*	0.11	0.20	0.19	0.07	0.06	0.11	0.06	0.43	0.13	0.03*
CaO	0.27	0.25	0.39	0.21	0.32	0.25	0.31	0.30	0.44	0.30	0.27	0.34	0.37
Na ₂ O	4.53	4.33	5.02	4.35	5.18	4.57	5.24	5.16	5.51	4.67	4.77	4.97	4.98
K ₂ O	10.2	10.7	9.23	10.5	9.08	10.1	9.16	9.30	8.73	10.1	9.78	9.62	9.43
<hr/>													
Total	99.4	99.3	98.4	99.6	99.9	100.3	98.9	98.6	99.4	99.3	99.3	99.5	99.3
An**	1.3	1.2	1.9	1.0	1.6	1.2	1.5	1.4	2.1	1.4	1.3	1.6	1.8
Ab**	39.7	37.7	44.4	38.3	45.7	40.2	45.8	45.1	47.9	40.6	42.0	43.3	43.7
Or**	59.0	61.1	53.7	60.7	52.7	58.6	52.7	53.5	50.0	58.0	56.7	55.1	54.5
Na/K (molecular)	0.673	0.618	0.826	0.631	0.867	0.686	0.869	0.843	0.959	0.701	0.741	0.785	0.803
<u>Notes:</u>	2	1	1	1	2	1	1	2	1	1	1	1	1

Explanation of Notes: * Amounts shown are as reported, but are below detection limit for an individual analysis.

** Feldspar endmembers, molecular proportions, normalized to 100%

1. Sanidine of typical composition (core analyses)

2. Sanidine "rim" composition

Table A-6: Electron Microprobe Analyses (in wt%) of Biotite Phenocrysts

<u>Analysis Number</u>	<u>1</u>	<u>2</u>	<u>3</u>	<u>4</u>	<u>5</u>	<u>6</u>	<u>7</u>	<u>8</u>
Sample	7Y-1	7Y-1	27X	27X	39X	39X	39X	39X
# points avgd.	6	6	5	1	6	3	5	2
<u>Oxide Wt %</u>								
SiO ₂	35.3	35.5	34.6	32.6	33.9	35.7	35.2	36.2
TiO ₂	4.52	4.67	4.56	5.41	4.50	4.66	4.61	4.75
Al ₂ O ₃	13.4	13.7	12.8	12.7	12.6	12.9	12.8	13.3
Cr ₂ O ₃	0.0*	0.01*	0.0*	0.0*	0.02*	0.01*	0.02*	0.01*
FeO	20.9	24.6	24.2	26.9	25.6	23.2	23.3	20.9
MnO	0.90	1.48	1.12	1.61	0.72	0.51	0.72	0.61
MgO	9.67	6.35	7.10	5.91	9.25	11.0	9.90	11.5
CaO	0.07	0.07	0.04	0.07	0.03	0.01*	0.04	0.05
Na ₂ O	0.32	0.29	0.35	0.33	0.44	0.54	0.43	0.49
K ₂ O	8.43	8.20	8.30	7.62	8.42	8.75	8.63	8.78
<u>Total</u>	<u>93.5</u>	<u>94.9</u>	<u>93.1</u>	<u>93.2</u>	<u>95.5</u>	<u>97.3</u>	<u>95.7</u>	<u>96.6</u>
Molecular								
Mg/(Mg+Fe)	0.45	0.32	0.34	0.28	0.39	0.46	0.43	0.50
<u>Notes:</u>	2	2	2	2	2	2	2	1

Explanation of Notes: * Amounts shown are as reported, but are below detection limit for an individual analysis.

- 1: "High Magnesium" Biotite
- 2: "Low Magnesium" Biotite

Table A-7: Electron Microprobe Analyses (in wt%) of Iron/Titanium Oxides

Analysis Number	1	2	3	4	5	6	7
Sample	33Z	33Z	33Z	33Z	33Z	33Z	31Y
Point Designation	O _{3A}	O _{3B}	O _{3C}	O ₅	O ₇	O ₈	O ₁
# points avgd.	1	1	2	2	2	2	4
Magnetites (Oxide Wt %)							
SiO ₂	0.16	0.15	0.39	0.12	0.35	0.18	0.08
TiO ₂	9.93	7.15	10.03	9.26	9.54	9.61	9.58
Al ₂ O ₃	1.50	1.76	1.51	1.18	1.54	1.63	1.45
Cr ₂ O ₃	0.05	0.05	0.05	0.05	0.04	0.05	0.01*
FeO	79.4	81.9	77.4	82.9	78.0	79.9	80.6
(FeO)	(37.9)	(35.4)	(37.6)	(39.2)	(37.1)	(38.1)	(37.8)
(Fe ₂ O ₃)	(46.2)	(51.7)	(44.2)	(48.6)	(45.6)	(46.5)	(47.6)
MnO	2.11	2.19	2.14	0.38	2.26	1.67	1.85
MgO	0.05	0.03	0.07	0.0*	0.06	0.03	0.08
CaO	0.02	0.02	0.04	0.03	0.04	0.03	0.02
Total	93.2(97.9)	93.3(98.5)	91.6(96.0)	93.9(98.8)	91.8(96.5)	93.1(97.8)	93.7(98.5)
XUSP^b	.299/.275	.215/.186	.310/.285	.282/.281	.293/.267	.295/.272	.286/.264
Point Designation	O ₂	O ₄					O ₆
# points avgd.	1	3					1
Ilmenites (Oxide wt.%)							
SiO ₂	0.02	0.02					0.04
TiO ₂	47.5	46.2					48.5
Al ₂ O ₃	0.06	0.08					0.15
Cr ₂ O ₃	0.01*	0.02					0.0*
FeO	40.26	47.1					42.2
(FeO)	(32.8)	(37.6)					(41.2)
(Fe ₂ O ₃)	(8.30)	(10.6)					(1.46)
MnO	9.68	3.63					2.26
MgO	0.03	0.17					0.06
CaO	0.07	0.02					0.06
Total	97.6(98.5)	97.2(98.3)					93.3(93.7)
XILM^b	.909/.808	.892/.888					.985/.984

Explanation of Notes: * Amounts shown are as reported, but are below detection limit for an individual analysis.

a: FeO and Fe₂O₃ and recalculated total (in parentheses) is based on recalculation of FeO to maintain stoichiometry.

b: XUSP and XILM are mole fractions of ulvospinel in magnetite and ilmenite in ilmenite/hematite, calculated by methods of Stormer and Lindsley, respectively. Lindsley values used in geothermometry.

APPENDIX B

Calibrations of Mechanical Property Measurement Devices

Each test system load cell is calibrated once a year against a standard transducer that is traceable to the U. S. Bureau of Standards (USBS). Before each test series, the axial displacement gages and the transverse displacement gages were calibrated with a calibrator (also traceable to the USBS) designed by McNamee (1985). Calibrations of the experimental methods and of the entire instrumentation setup were obtained preceding and following each sub-series by testing an aluminum sample of known mechanical properties. All of these calibration checks were run on 6061-T651 aluminum cylinders (like-sized to the rock samples) with a Young's modulus (E) of 69.7 GPa and a Poisson's ratio (ν) of 0.33.

As has been the case in all previous reports on mechanical properties of intact tuff for the NNWSI project (Price and Jones, 1982; Price, Jones, and Nimick, 1982; Price and Nimick, 1982; Price, Nimick, and Zirzow, 1982; Price, Spence, and Jones, 1984; Price, et al., 1985; Nimick, et al., 1985; Price, 1986; Nimick, VanBuskirk, and MacFarland, in preparation), all measured values taken during gage calibrations are within 5% of actual values. Also, all pre- and post-test aluminum calibration checks resulted in measured elastic properties of aluminum within 5% of the published, ideal values.

The gage calibration sheets and test records from the aluminum calibration checks are on file in the Geomechanics Division at Sandia National Laboratories.

APPENDIX C

The following portions of this document are candidate information for the NNWSI Tuff Data Base (TDB):

Normative Mineralogy Data, p.13.

Feldspar Compositions, p.13-14.

Temperature Data, p.14-15.

Oxygen Fugacity Data, p.15.

Percent Silica Minerals, p.16.

Tables 3, 4, and 5.

Tables A-1 through A-7.

APPENDIX D

This report contains do data taken from or that should be included in the NNWSI Reference Information Base (RIB).

DISTRIBUTION LIST

B. C. Rusche, Director (RW-1)
Office of Civilian Radioactive
Waste Management
U. S. Department of Energy
Forrestal Building
Washington, D. C. 20585

R. Stein (RW-23)
Office of Civilian Radioactive
Waste Management
U. S. Department of Energy
Forrestal Building
Washington, D. C. 20585

J. J. Fiore (RW-221)
Program Management Division
Office of Civilian Radioactive
Waste Management
U. S. Department of Energy
Forrestal Building
Washington, D. C. 20585

M. W. Frei (RW-231)
Office of Civilian Radioactive
Waste Management
U. S. Department of Energy
Forrestal Building
Washington, D. C. 20585

E. S. Burton (RW-25)
Siting Division
Office of Geologic Repositories
U. S. Department of Energy
Forrestal Building
Washington, D. C. 20585

C. R. Cooley (RW-24)
Geosciences & Technology Division
Office of Geologic Repositories
U. S. Department of Energy
Forrestal Building
Washington, D. C. 20585

V. J. Cassella (RW-22)
Office of Civilian Radioactive
Waste Management
U. S. Department of Energy
Forrestal Building
Washington, D. C. 20585

T. P. Longo (RW-25)
Program Management Division
Office of Geologic Repositories
U. S. Department of Energy
Forrestal Building
Washington, D. C. 20585

C. Klingsberg (RW-24)
Geosciences & Technology Division
Office of Geologic Repositories
U. S. Department of Energy
Forrestal Building
Washington, D. C. 20585

B. G. Gale (RW-25)
Siting Division
Office of Civilian Radioactive
Waste Management
U. S. Department of Energy
Forrestal Building
Washington, D. C. 20585

R. J. Blaney (RW-22)
Program Management Division
Office of Geologic Repositories
U. S. Department of Energy
Forrestal Building
Washington, D. C. 20585

R. W. Gale (RW-40)
Office of Civilian Radioactive
Waste Management
U. S. Department of Energy
Forrestal Building
Washington, D. C. 20585

J. E. Shaheen (RW-44)
Outreach Programs
Office of Policy, Integration,
and Outreach
U. S. Department of Energy
Forrestal Building
Washington, D. C. 20585

J. O. Neff, Manager
Salt Repository Project Office
U. S. Department of Energy
505 King Avenue
Columbus, OH 43201

D. C. Newton (RW-23)
Engineering & Licensing Division
Office of Geologic Repositories
U. S. Department of Energy
Forrestal Building
Washington, D. C. 20585

O. L. Olson, Manager
Basalt Waste Isolation Project Office
Richland Operations Office
U. S. Department of Energy
Post Office Box 550
Richland, WA 99352

D. L. Vieth, Director (4)
Waste Management Project Office
U. S. Department of Energy
Post Office Box 14100
Las Vegas, NV 89114

D. F. Miller, Director
Office of Public Affairs
U. S. Department of Energy
Post Office Box 14100
Las Vegas, NV 89114

P. M. Bodin (12)
Office of Public Affairs
U. S. Department of Energy
Post Office Box 14100
Las Vegas, NV 89114

B. W. Church, Director
Health Physics Division
U. S. Department of Energy
Post Office Box 14100
Las Vegas, NV 89114

Chief, Repository Projects Branch
Division of Waste Management
U. S. Nuclear Regulatory Commission
Washington, DC 20555

Document Control Center
Division of Waste Management
U. S. Nuclear Regulatory Commission
Washington, DC 20555

S. A. Mann, Manager
Crystalline Rock Project Office
U. S. Department of Energy
9800 South Cass Avenue
Argonne, IL 60439

K. Street, Jr.
Lawrence Livermore National Laboratory
Post Office Box 808
Mail Stop L-209
Livermore, CA 94550

L. D. Ramspott (3)
Technical Project Officer for NNWSI
Lawrence Livermore National Laboratory
Post Office Box 808
Mail Stop L-204
Livermore, CA 94550

W. J. Purcell (RW-20)
Associate Director
Office of Civilian Radioactive
Waste Management
U. S. Department of Energy
Forrestal Building
Washington, D. C. 20585

D. T. Oakley (4)
Technical Project Officer for NNWSI
Los Alamos National Laboratory
Post Office Box 1663
Mail Stop F-619
Los Alamos, NM 87545

L. R. Hayes (3)
Technical Project Officer for NNWSI
U. S. Geological Survey
Post Office Box 25046
421 Federal Center
Denver, CO 80225

NTS Section Leader
Repository Projects Branch
Division of Waste Management
U. S. Nuclear Regulatory Commission
Washington, DC 20555

V. M. Glanzman
U. S. Geological Survey
Post Office Box 25046
913 Federal Center
Denver, CO 80225

P. T. Prestholt
NRC Site Representative
1050 East Flamingo Road
Suite 319
Las Vegas, NV 89109

M. E. Spaeth
Technical Project Officer for NNWSI
Science Applications International, Corp.
101 Convention Center Drive, Suite 407
Las Vegas, NV 89109

SAIC-T&MSS Library (2)
Science Applications International, Corp.
101 Convention Center Drive
Las Vegas, NV 89109

W. S. Twenhofel, Consultant
Science Applications International, Corp.
820 Estes Street
Lakewood, CO 80215

A. E. Gurrola, General Manager
Energy Support Division
Holmes & Narver, Inc.
Post Office Box 14340
Las Vegas, NV 89114

J. A. Cross, Manager
Las Vegas Branch
Fenix & Scisson, Inc.
Mail Stop 514
Post Office Box 14308
Las Vegas, NV 89114

N. Duncan (RW-44)
Office of Policy, Integration,
and Outreach
U. S. Department of Energy
Forrestal Building
Washington, D. C. 20585

J. Fordham
Desert Research Institute
Water Resources Center
Post Office Box 60220
Reno, NV 89506

J. S. Wright
Technical Project Officer for NNWSI
Westinghouse Electric Corporation
Waste Technology Services Division
Nevada Operations
Post Office Box 708
Mail Stop 703
Mercury, NV 89023

ONWI Library
Battelle Columbus Laboratory
Office of Nuclear Waste Isolation
505 King Avenue
Columbus, OH 43201

W. M. Hewitt, Program Manager
Roy F. Weston, Inc.
955 L'Enfant Plaza SW, Suite 800
Washington, DC 20024

H. D. Cunningham, General Manager
Reynolds Electrical & Engineering Company,
Inc.
Post Office Box 14400
Mail Stop 555
Las Vegas, NV 89114

T. Hay, Executive Assistant
Office of the Governor
State of Nevada
Capitol Complex
Carson City, NV 89710

R. R. Loux, Jr., Director (3)
Nuclear Waste Project Office
State of Nevada
Evergreen Center, Suite 252
1802 North Carson Street
Carson City, NV 89701

**C. H. Johnson, Technical
Program Manager**
Nuclear Waste Project Office
State of Nevada
Evergreen Center, Suite 252
1802 North Carson Street
Carson City, NV 89701

Dr. M. Mifflin
Desert Research Institute
Water Resources Center
Suite 1
2505 Chandler Avenue
Las Vegas, NV 89120

Department of Comprehensive Planning
Clark County
225 Bridger Avenue, 7th Floor
Las Vegas, NV 89155

Lincoln County Commission
Lincoln County
Post Office Box 90
Pioche, NV 89043

Community Planning and Development
City of North Las Vegas
Post Office Box 4086
North Las Vegas, NV 89030

City Manager
City of Henderson
Henderson, NV 89015

N. A. Norman
Project Manager
Bechtel National Inc.
Post Office Box 3965
San Francisco, CA 94119

F. Butler
Los Alamos Technical Associates
1650 Trinity Drive
Los Alamos, NM 87544

T. G. Barbour
Science Applications
International Corporation
1626 Cole Boulevard, Suite 270
Golden, CO 80401

Planning Department
Nye County
Post Office Box 153
Tonopah, NV 89049

Economic Development Department
City of Las Vegas
400 East Stewart Avenue
Las Vegas, NV 89101

Director of Community Planning
City of Boulder City
Post Office Box 367
Boulder City, NV 89005

Commission of European Communities
200 Rue de la Loi
B-1049 Brussels
BELGIUM

Technical Information Center
Roy F. Weston, Inc.
955 L'Enfant Plaze, SW, Suite 800
Washington, DC 20024

R. Harig
Parsons, Brinkerhoff, Quade, &
Douglass, Inc.
1625 Van Ness Avenue
San Francisco, CA 94109-3678

Dr. M. M. Singh, President
Engineers International, Inc.
98 East Naperville Road
Westmont, IL 60559-1595

Dr. N. L. Carter, Director
Center for Tectonophysics
Texas A& M University
College Station, TX 77843

RE/SPEC, Inc. (2)
Post Office Box 725
Rapid City, SD 57701
Attention:
P. F. Gnirk
P. E. Senseny

RE/SPEC, Inc. (2)
Post Office Box 14984
Albuquerque, NM 87191
Attention:
S. W. Key
D. K. Parrish

R. Coppage, Senior Mining Engineer
Fenix & Scisson, Inc.
Post Office Box 498
Mercury, NV 89023

C. Barton
U. S. Geological Survey
Post Office Box 327
Mercury, NV 89023

E. P. Binnall
Field Systems Group
Building 50B/4235
Lawrence Berkeley Laboratory
University of California
Berkeley, CA 94720

J. D. Blacic
Los Alamos National Laboratory
Post Office Box 1663
Mail Stop J-980
Los Alamos, NM 87545

R. E. Riecker
Los Alamos National Laboratory
Post Office Box 1663
Group ESS-3
Los Alamos, NM 87545

R. Newmark
Lawrence Livermore National Laboratory
Post Office Box 808
Mail Stop L-221
Livermore, CA 94550

T. H. Isaacs (RW-22)
Office of Geologic Repositories
U. S. Department of Energy
Forrestal Building
Washington, D. C. 20585

D. H. Alexander (RW-232)
Office of Geologic Repositories
U. S. Department of Energy
Forrestal Building
Washington, D. C. 20585

J. P. Knight (RW-24)
Office of Civilian Radioactive
Waste Management
U. S. Department of Energy
Forrestal Building
Washington, D. C. 20585

A. Jelacic (RW-233)
Office of Civilian Radioactive
Waste Management
U. S. Department of Energy
Forrestal Building
Washington, D. C. 20585

G. Parker (RW-241)
Office of Civilian Radioactive
Waste Management
U. S. Department of Energy
Forrestal Building
Washington, D. C. 20585

J. R. Rollo
Deputy Assistant Director
for Engineering Geology
U. S. Geological Survey
106 National Center
12201 Sunrise Valley Drive
Reston, VA 22092

B. J. King, Librarian (2)
Basalt Waste Isolation Project Library
Rockwell Hanford Operations
Post Office Box 800
Richland, WA 99352

C. M. St. John
J. F. T. Agapito Associates, Inc.
27520 Hawthorne Blvd., Suite 137
Rolling Hills Estates, CA 90274

Roger Hart
Itasca Consulting Group, Inc.
Post Office Box 14806
Minneapolis, MN 55414

D. Fenster
Roy F. Weston, Inc.
955 L'Enfant Plaza SW
Washington, DC 20024

C. Voss
Batelle
2030 M St. NW, Suite 800
Washington, DC 20036

E. Hardin
Science Applications International, Corp.
101 Convention Center Drive, Suite 409
Las Vegas, NV 89109

D. Eppler
Science Applications International, Corp.
101 Convention Center Drive, Suite 409
Las Vegas, NV 89109

J. R. Connolly (20)
Department of Geology
Institute of Meteoritics
University of New Mexico
Albuquerque, NM 87131

D. L. Fraser, General Manager
Reynolds Electrical & Engineering Company,
Inc.
Post Office Box 14400
Mail Stop 555
Las Vegas, NV 89114-4400

V. Gong
Technical Project Officer for NNWSI
Reynolds Electrical & Engineering Company,
Inc.
Post Office Box 14400
Mail Stop 615
Las Vegas, NV 89114-4400

R. L. Mundell
United States Bureau of Mines
Post Office Box 25086
Building 20
Denver Federal Center
Denver, CO 80225

R. J. Martin, III
New England Research, Inc.
Post Office Box 857
Norwich, VT 05055

J. P. Pedalino
Technical Project Officer for NNWSI
Holmes & Narver, Inc.
Mail Stop 605
Post Office Box 14340
Las Vegas, NV 89114

S. H. Kale (RW-20)
Office of Civilian Radioactive
Waste Management
U. S. Department of Energy
Forrestal Building
Washington, D. C. 20585

S. D. Murphy
Technical Project Officer for NNWSI
Fenix & Scisson, Inc.
Mail Stop 514
Post Office Box 15408
Las Vegas, NV 89114

J. H. Anttonen
Deputy Assistant Manager for
Commercial Nuclear Waste
Basalt Waste Isolation Project Office
Richland Operations Office
U. S. Department of Energy
Post Office Box 550
Richland, WA 99352

E. Anderson
Mountain West Research-Southwest, Inc.
398 South Mill Avenue, Suite 300
Tempe, AZ 85281

J. Foremaster (5)
City of Caliente
Post Office Box 158
Caliente, NV

1510 J. W. Nunziato
 1520 D. J. McCloskey
 1521 R. D. Krieg
 1530 L. W. Davison
 1540 W. C. Luth
 1541 H. C. Hardee
 1542 S. R. Brown
 1542 D. J. Holcomb
 1542 W. A. Olsson
 1542 L. W. Teufel
 1542 W. R. Wawersik
 1542 D. H. Zeuch
 1543 T. M. Gerlach
 3141 S. A. Landenberger (5)
 3151 W. L. Garner (3)
 3154-3 C. H. Dalin, for DOE/OSTI (28)
 6300 R. W. Lynch
 6310 T. O. Hunter
 6310 NNWSICF
 6311 V. Hinkel (2)
 6311 C. Mora
 6311 A. Stevens
 6312 F. W. Bingham
 6312 B. S. Langkopf
 6313 T. E. Blejwas
 6313 R. Finley
 6313 E. A. Klavetter
 6313 F. B. Nimick
 6313 R. H. Price (25)
 6313 B. M. Schwartz (4)
 L02A1.A-08/04/83
 L02A1.A-12/05/84
 L02A1.A-06/26/85
 L04.A-02/13/84
 6313 L. E. Shephard
 6313 R. M. Zimmerman
 6314 S. J. Bauer
 6314 L. S. Costin
 6314 B. L. Ehgartner
 6314 A. J. Mansure
 6314 J. R. Tillerson
 6315 S. Sinnock
 6332 WMT Library (20)
 6430 N. R. Ortiz
 8024 P. W. Dean



Sandia National Labs